REVIEW

Open Access

Reconstruction of skin friction topology in complex separated flows

Tianshu Liu[1*]

*Correspondence:
tianshu.liu@wmich.edu

[1] Department of Mechanical and Aerospace Engineering, Western Michigan University, Kalamazoo, MI 49008, USA

Abstract

This paper describes a theoretical method for reconstruction of the skin friction topology in complex separated flows, which is developed based on the exact relation between skin friction and surface pressure through the boundary enstrophy flux (BEF). The key of this method is that a skin friction field is reconstructed from a surface pressure field as an inverse problem by applying a variational method. For applications, the approximate method is proposed, where the composite surface pressure field is given by a linear superposition of the base-flow surface pressure field and the surface pressure variation field and the base-flow BEF field is used as the first-order approximation. This approximate method is constructive in a mathematical sense since a complex skin friction field in separated flows can be reconstructed from some elemental skin friction structures (skin friction source/sink, vortex and their combinations) by a linear superposition of some simple surface pressure structures. The distinct topological features, such as critical points, separation lines and attachment lines, naturally occur as a result of such reconstruction. As examples, some elemental skin friction structures in separated flows are reconstructed in simulations, and the skin friction fields in shock-wave/boundary-layer interactions (SWBLIs) are reconstructed from pressure sensitive paint (PSP) images obtained in wind tunnel experiments.

Keywords: Skin friction, Surface pressure, Boundary enstrophy flux, Flow separation, Topology, Inverse problem, Variational method, Euler–Lagrange equation, Taylor-series-expansion solution, Navier–Stokes equations, Poincare-Bendixson index formula, Shock-wave/boundary-layer interaction, Pressure sensitive paint, Aerodynamics

1 Introduction

Three-dimensional (3D) separated flows are characterized by the skin friction topology featured with isolated critical points (nodes and saddles), separation lines and attachment lines. Skin friction is one of the fundamental surface quantities (along with surface pressure) in fluid mechanics and aerodynamics. The skin friction topology reveals near-wall structures of complex flows. In experiments, to study the skin friction topology, surface oil-streak visualizations are often conducted, and then the topological structures are identified and conjectured from oil-streak patterns based on observer's intuition and experience. However, it is difficult to unambiguously infer some topological structures (particularly saddles and attachment lines) in skin friction fields by directly observing surface flow

visualizations without quantitative image processing and analysis. To deal with this problem, the critical-point theory in differential dynamical systems, differential geometry and surface topology can be adopted to provide a natural framework for a description of the flow topology (or the skin friction topology). Legendre [1] and Lighthill [2] considered the critical-point theory as a rational framework to describe the skin friction topology in 3D separated flows. The topological analysis on the critical points has been elaborated as a tool in the experimental and computational studies of various separated flows [3–15].

Lighthill [2] pointed out the applicability of the Poincare-Hopf index theorem as a topological constraint on a skin friction field. Hunt et al. [4] extended this approach and proposed the topological rules for several separated flow cases. It is generally accepted that these topological rules are valid as the consequences of the Poincare-Hopf index theorem, and applicable to flow visualizations as necessary constraints to identify some hidden critical points that cannot be directly observed in visualizations. Ma and Wang [16] gave a generalized Poincare-Hopf index theorem for a vector field on a manifold with a non-penetrable boundary, which led to a topological rule for 2D incompressible flow that is similar to that given by Hunt et al. [4]. Foss [14, 15] applied the Poincare-Hopf index theorem to a collapsed sphere with the lateral edges called seams where vectors are required to be tangential to the boundary and considered inflow and outflow across the boundary through holes on the sphere. Further, considering a penetrable boundary in a skin friction field, Liu et al. [17] applied the Poincare-Bendixson index formula (the P-B formula in short) to various separated flow cases, presenting a conservation law between isolated critical points and boundary switch points. The classical results, such as the hairy sphere theorem [18, 19], the topological rule given by Hunt et al. [4] for junction flows, and Foss' collapsed sphere method [14, 15], can be derived from the P-B formula.

Near-wall flow structures are directly related to the features of skin friction (τ) and surface pressure (p), which are critical to understand the physics of 3D wall-bounded complex flows. To reconstruct a near-wall velocity field, a Taylor-series-expansion solution near a wall in an incompressible viscous flow can be sought by solving the Navier–Stokes (NS) equations [6, 20]. The coefficients in the series-expansion solution are constrained by the NS equations and the continuity equation with the no-slip boundary condition [21, 22]. This Taylor-series-expansion method allows reconstruction of several typical near-wall flow structures observed in 3D separated flows, indicating that a near-wall velocity field is solely determined by the skin friction and surface pressure fields (simply called the τ- and p-fields) [21, 22]. Further, the τ- and p-fields are intrinsically coupled through the boundary enstrophy flux (BEF), providing an extra constraint on near-wall flows [23, 24]. From a theoretical perspective, reconstruction of (τ, p)-structures is critical in order to understand near-wall flows, which is also useful for extracting a τ-field from a p-field obtained in pressure sensitive paint (PSP) measurements in high-speed wind tunnels.

Currently, the topological analysis and Taylor-series-expansion solution of the NS equations are the main tools for the studies of complex separated flows when the τ- and p-fields are known in experiments and computations. However, our understanding of complex separated flows is still very limited. First, a τ-field in complex flows is notoriously difficult to determine accurately in experiments and computations [25, 26].

Furthermore, the existing qualitative theories focusing on the criteria of boundary layer separations and admissible types of skin friction patterns [27–30] do not provide a convenient and feasible way for reconstruction of complex separated flows. Therefore, it is highly desirable to develop a theoretical method that is constructive in a mathematical sense for reconstruction of different types of separated flows in the theoretical and experimental analyses.

More specifically, an intriguing question is whether a τ-field in a complex separated flow could be reconstructed from a p-field obtained by superposition of some elemental p-structures such that the near-wall flow structures could be further reconstructed by using the Taylor-series-expansion solution of the NS equations. Liu et al. [31] developed a theoretical method for reconstruction of a τ-field from a p-field that is given by superposing the elemental p-structures that occur in complex separated flows. This constructive method has several technical aspects. First, the on-wall relation between τ and p through the boundary enstrophy flux (BEF) is derived from the NS equations, which provides a rational foundation for reconstruction of a τ-field from a p-field in complex flows [23, 24]. When the BEF is given (modeled and approximated), a variational method is developed to reconstruct a τ-field from a p-field as an inverse problem by solving the Euler–Lagrange equation. Further, an approximate method is developed based on a base flow with the known BEF, where the pressure field is a superposition of the base-flow surface pressure field and a surface pressure variation and the base-flow BEF is used as a first-order approximation. This approximate method has been applied to reconstruction of the elemental τ-structures, including τ-source/sink, τ-vortex and their combinations for complex separated flows [31]. Using the approximate method, Liu et al. [32, 33] determined skin friction fields in incident and swept shock-wave/boundary-layer interactions (SWBLIs) based on unsteady PSP images obtained in experiments in supersonic wind tunnels.

This paper is organized as follows. After Introduction, in Section 2, the relevant theoretical aspects of the developed constructive method are described, including the exact relation between skin friction and surface pressure through the BEF, the variational method and Euler–Lagrange equation, the approximate method with the superposed surface pressure field and the base-flow BEF field, the Taylor-series-expansion solution of the NS equations, and the Poincare-Bendixson index formula. In Section 3, reconstruction of the elemental (τ, p)-structures is discussed, including the base flow with the power-law distributions, τ-source/sink, τ-vortex and their combinations. In Section 4, more complex (τ, p)-structures are reconstructed in SWBLIs and the flow over a delta wing. In Section 5, the τ-fields in incident and swept SWBLIs are reconstructed from PSP images obtained in experiments, revealing the near-2D and conical separation bubbles and the formation of the secondary separation bubble (SSB). Finally, the conclusions are made.

2 Relevant aspects of a constructive method

2.1 Relation between skin friction and surface pressure

Although τ and p are conventionally treated as two independent quantities, there is in fact an exact relation between τ and p in viscous flows. This on-wall relation between p and τ was derived from the NS equations by Liu et al. [23] using the Taylor-series expansion method and Chen et al. [24] using the method of differential geometry.

Theoretically, the coupling structures of τ and p reveal coherent near-wall structures in complex flows since near-wall velocity can be completely reconstructed from τ and p by using the Taylor-series-expansion solution of the NS equations [21, 22]. On the other hand, from a standpoint of measurement, this coupling relation between τ and p can be used to extract the τ-fields from PSP measurements.

This on-wall relation in a compressible viscous flow is written in a vector form, i.e., [23, 24]

$$\tau \cdot \nabla_{\partial B} p = \mu f_{\Omega}, \tag{1}$$

where f_{Ω} acts as a source term, which is expressed as

$$f_{\Omega} = \mu \left[\frac{\partial \Omega}{\partial n}\right]_{\partial B} - \mu \boldsymbol{\omega}_{\partial B} \cdot \boldsymbol{K} \cdot \boldsymbol{\omega}_{\partial B} + \mu_{\theta}(\boldsymbol{\omega}_{\partial B} \times \boldsymbol{n}) \cdot \nabla_{\partial B}\theta_{\partial B}, \tag{2}$$

where $\Omega = |\boldsymbol{\omega}|^2/2$ is the enstrophy, $\partial/\partial n$ is the wall-normal derivative, $\boldsymbol{\omega} = \nabla \times \boldsymbol{u}$ is the vorticity, $\boldsymbol{K}$ is the surface curvature tensor, $\theta = \nabla \cdot \boldsymbol{u}$ is the dilation rate, μ is the dynamic viscosity, μ_{θ} is the longitudinal viscosity, $\nabla_{\partial B}$ is a gradient operator on a surface, and $\boldsymbol{n}$ is the unit normal vector of the surface. The subscript ∂B in the variables and operators in Eq. (2) denotes the quantities on the surface.

Equation (1) represents a formal balance between the surface pressure gradient $\nabla_{\partial B} p$ projected on the skin friction vector τ and the scalar quantity f_{Ω} that is originated from the diffusion term in the NS equations. In Eq. (2), the first term $\mu[\partial\Omega/\partial n]_{\partial B}$ is the boundary enstrophy flux (BEF) and the second term is interpreted as the curvature-induced contribution. The term $\boldsymbol{\omega}_{\partial B} \cdot \boldsymbol{K} \cdot \boldsymbol{\omega}_{\partial B}$ in Eq. (2) is formally interpreted as the interaction between the surface curvature and the vorticity on a surface. The quadratic form $\boldsymbol{\omega}_{\partial B} \cdot \boldsymbol{K} \cdot \boldsymbol{\omega}_{\partial B}$ can be transformed into the standard form $\boldsymbol{\omega}_{\partial B} \cdot \boldsymbol{K} \cdot \boldsymbol{\omega}_{\partial B} = \kappa_1\omega_1^2 + \kappa_2\omega_2^2$ with the two principal curvatures κ_1 and κ_2, where $\omega_1 = \boldsymbol{\omega}_{\partial B} \cdot \boldsymbol{e}_1$ and $\omega_2 = \boldsymbol{\omega}_{\partial B} \cdot \boldsymbol{e}_2$ are the vorticity components on the principal directions $\boldsymbol{e}_1$ and $\boldsymbol{e}_2$. For a concave surface with $\kappa_1 \leq 0$ and $\kappa_2 < 0$ (such as concave ellipsoid and cylinder), $\boldsymbol{\omega}_{\partial B} \cdot \boldsymbol{K} \cdot \boldsymbol{\omega}_{\partial B} < 0$. For a convex surface with $\kappa_1 \geq 0$ and $\kappa_2 > 0$ (such as convex ellipsoid and cylinder), $\boldsymbol{\omega}_{\partial B} \cdot \boldsymbol{K} \cdot \boldsymbol{\omega}_{\partial B} > 0$. For a hyperboloid surface with $\kappa_1 > 0$ and $\kappa_2 < 0$, the sign of $\boldsymbol{\omega}_{\partial B} \cdot \boldsymbol{K} \cdot \boldsymbol{\omega}_{\partial B}$ is undetermined. The ratio between the magnitudes of the second and first terms (the curvature and BEF terms) in Eq. (2) is proportional to δ_c/R_s, where δ_c is the viscous diffusion length scale and R_s is defined as the mean curvature radius of the surface. When the Reynolds number is sufficiently large such that $\delta_c/R_s \ll 1$, the second term in Eq. (2) could be neglected. In this case, f_{Ω} is dominated by the BEF. The third term is interpreted as the contribution induced by the temporal-spatial change of the fluid density on the surface, which is zero in an incompressible flow.

2.2 Variational solution

Here, a key problem is how to extract a τ-field from a p-field by solving Eq. (1) as an inverse problem when a f_{Ω}-field is given, which is similar to the optical flow problem [34–36]. In the orthographic projection, the surface coordinates on a relatively flat surface are proportional to the image coordinates. Therefore, for convenience of image processing, computations for solving Eq. (1) are directly carried out in the image plane. This problem is ill-posed since there are two unknowns in the single equation, which belongs

to a large class of inverse problems in scientific and engineering fields. To deal with this problem, a variational formulation with a regularization constraint is used [34]. We consider the following functional on a domain D in the image plane for minimization, i.e.,

$$J(\boldsymbol{\tau}) = \int_D (G + \boldsymbol{\tau} \cdot \nabla p)^2 dx_1 dx_2 + \alpha \int_D \left(|\nabla \tau_1|^2 + |\nabla \tau_2|^2 \right) dx_1 dx_2. \tag{3}$$

Where $\boldsymbol{\tau} = (\tau_1, \tau_2)$ is a skin friction vector, $G = -\mu f_\Omega$ is a source term, α is a Lagrange multiplier that is a pre-set empirical constant in this case, $\nabla = (\partial/\partial x_1, \partial/\partial x_2)$ is the gradient operator in the image plane (i.e., $\nabla_{\partial B}$ projected on the image plane), and $x_i (i = 1, 2)$ are the image coordinates. The first term in $J(\boldsymbol{\tau})$ is the equation term. The second term in $J(\boldsymbol{\tau})$ is a regularization constraint term assuming that a $\boldsymbol{\tau}$-field is sufficiently continuous and smooth.

The optimality condition for $J(\boldsymbol{\tau}) \to$ min is

$$\begin{aligned} \left. \frac{dJ(\boldsymbol{\tau} + \varepsilon \boldsymbol{v})}{d\varepsilon} \right|_{\varepsilon=0} &= 2\int_D \left(w \nabla p - \frac{\alpha}{2} \nabla^2 \boldsymbol{\tau} \right) \cdot \boldsymbol{v} dx_1 dx_2 \\ &+ \alpha \int_D \nabla^2 (\boldsymbol{\tau} \cdot \boldsymbol{v}) dx_1 dx_2 - \alpha \int_D \boldsymbol{\tau} \cdot \nabla^2 \boldsymbol{v} dx_1 dx_2 = 0 \end{aligned},$$

where $w = G + \boldsymbol{\tau} \cdot \nabla p$ is the equation term, $\boldsymbol{v}$ is a variation (perturbation) to be specified, and ε is a small amplitude. Further, using Green's theorem, we know

$$\int_D \nabla^2 (\boldsymbol{\tau} \cdot \boldsymbol{v}) dx_1 dx_2 = \int_{\partial D} (\widehat{\boldsymbol{n}} \cdot \nabla \boldsymbol{\tau}) \cdot \boldsymbol{v} dl + \int_{\partial D} (\widehat{\boldsymbol{n}} \cdot \nabla \boldsymbol{v}) \cdot \boldsymbol{\tau} dl,$$

where $\widehat{\boldsymbol{n}}$ is a unit normal vector on a closed boundary ∂D of the domain D. We consider a variation field that satisfies the Laplace equation $\nabla^2 \boldsymbol{v} = 0$ with the Neumann condition $\widehat{\boldsymbol{n}} \cdot \nabla \boldsymbol{v} = 0$ on ∂D. Further, the Neumann condition $\widehat{\boldsymbol{n}} \cdot \nabla \boldsymbol{\tau} = \partial \boldsymbol{\tau}/\partial \widehat{n} = 0$ is imposed on ∂D for a $\boldsymbol{\tau}$-field. Therefore, we have

$$\left. \frac{dJ(\boldsymbol{\tau} + \varepsilon \boldsymbol{v})}{d\varepsilon} \right|_{\varepsilon=0} = 2\int_D \left(w \nabla p - \frac{\alpha}{2} \nabla^2 \boldsymbol{\tau} \right) \cdot \boldsymbol{v} dx_1 dx_2 = 0.$$

Since D is arbitrary and $\boldsymbol{v}$ is non-zero, the Euler–Lagrange equation is obtained, i.e.,

$$(G + \boldsymbol{\tau} \cdot \nabla p) \nabla p - \alpha \nabla^2 \boldsymbol{\tau} = 0, \tag{4}$$

where $\nabla^2 = \partial^2/\partial x_1^2 + \partial^2/\partial x_2^2$ is the Laplace operator (note that $\alpha/2$ is replaced by α since α is a free parameter). The Lagrange multiplier α in Eq. (4) acts as an artificial diffusion coefficient that tends to smooth out the solution when it is large. Given a p-field and a f_Ω-field, Eq. (4) can be solved numerically for a $\boldsymbol{\tau}$-field with the Neumann condition $\partial \boldsymbol{\tau}/\partial \widehat{n} = 0$ on ∂D. The standard finite difference method is used to solve Eq. (4), and the numerical algorithm is essentially the same as that for the optical flow problem [35–37]. The open-source Matlab program package for extraction of a $\boldsymbol{\tau}$-field from a p-field is available in the folder 'OpenSkinFrictionFromPressure_v1', which is in the GitHub site: https://github.com/Tianshu-Liu/Open_Global_Flow_Diagnostics.

In an error analysis, substitution of the decompositions $p = p_0 + \delta p$, $G = G_0 + \delta G$ and $\boldsymbol{\tau} = \boldsymbol{\tau}_0 + \delta \boldsymbol{\tau}$ to Eq. (4) yields an error propagation equation, where δp, δG and $\delta \boldsymbol{\tau}$ are errors of p, G and $\boldsymbol{\tau}$, respectively, and p_0, G_0 and $\boldsymbol{\tau}_0$ are the non-perturbed fields that exactly satisfy Eq. (4). A formal estimate of the relative skin friction error $(\delta \boldsymbol{\tau})_N = \delta \boldsymbol{\tau} \cdot \boldsymbol{N}_p$ is [25, 26]

$$\frac{(\delta\boldsymbol{\tau})_N}{\|\boldsymbol{\tau}_0\|} = -\frac{\delta G}{\|\nabla p_0\|\|\boldsymbol{\tau}_0\|} - \left(\frac{\boldsymbol{\tau}_0}{\|\boldsymbol{\tau}_0\|}\right)\cdot\delta\boldsymbol{N}_p + \frac{\alpha}{\|\nabla p_0\|^2}\nabla^2\left[\frac{(\delta\boldsymbol{\tau})_N}{\|\boldsymbol{\tau}_0\|}\right],$$ (5)

where $\|\|$ denotes a L^2-norm, $\|\boldsymbol{\tau}_0\|$ is a characteristic value of skin friction, and $\boldsymbol{N}_p = \nabla p_0/\|\nabla p_0\|$ is the unit surface pressure gradient that is normal to an iso-pressure line $p_0 = const.$. The first term in the right-hand side (RHS) of Eq. (5) is the contribution from the elemental error in measurement of G. The second term is the contribution from the elemental error in measurement of the surface gradient of p. The third term is the contribution from the artificial diffusion of $(\Delta\boldsymbol{\tau})_N$ associated with the Lagrange multiplier. Since the first term in the RHS of Eq. (5) is proportional to $\|\nabla p_0\|^{-1}$, the relative error $(\Delta\boldsymbol{\tau})_N/\|\boldsymbol{\tau}_0\|$ increases as $\|\nabla p_0\|$ decreases. The third term is proportional to $\alpha\|\nabla p_0\|^{-2}$, indicating that the Lagrange multiplier α must be sufficiently small to reduce the error, particularly when $\|\nabla p_0\|$ is small.

On the other hand, for an ill-posed inverse problem, the variational solution with the Lagrange multiplier α is affected by the data error bounded by a positive number δ. The error of the solution is proportional to $\delta/\sqrt{\alpha}$ as $\delta \to 0$ [25, 26]. The selected value of α depends on δ, i.e., $\alpha = \alpha(\delta)$, which is implied in Eq. (5). The condition for the solution convergence is $\delta^2/\alpha(\delta) \to 0$, indicating that the data error must be reduced when α is small. Therefore, two conflicting requirements exit to obtain a smooth and accurate solution. In the regions where $\|\nabla p_0\|$ is small, α should be small based on Eq. (5), and accordingly the data error bound δ must be tightly controlled to insure the accuracy of the solution. From this perspective, there may be the optimum value of α. No rigorous theory is available to determine the optimum value of α a priori. The selection of α is a trial-and-error procedure based on simulations for a specific application.

2.3 Approximate method

Equation (1) is exactly valid instantaneously in relating $\boldsymbol{\tau}$ to p through f_Ω. The limitation in applying this equation to extract skin friction is to determine the BEF that is defined in the f_Ω term in Eq. (2). In theoretical cases where the BEF is known a priori, the variational solution for this inverse problem is feasible [23]. Unfortunately, for complex flows, the BEF is a difficult quantity to measure experimentally or determine theoretically. Since a f_Ω-field is generally unknown, the solution of Eq. (4) for a $\boldsymbol{\tau}$-field in complex flows cannot be readily obtained for a given p-field only. This problem is considered as a closure problem in which modeling of f_Ω is required. A successive approximation is proposed to obtain a $\boldsymbol{\tau}$-field induced by a surface-pressure variation imposed on a base flow [31]. Figure 1 shows a flowchart of the iterative approximate method. First, a known base flow is considered, which satisfies the basic relation $\boldsymbol{\tau}^{(0)}\cdot\nabla p^{(0)} = \mu f_\Omega^{(0)}$, where the superscript '0' denotes the base flow as the zeroth-order approximation. In applications, a base flow could be a relatively simple known steady attached flow such as a boundary layer.

Consider a physical situation in which a surface-pressure variation is suddenly imposed on the base flow through a certain external process such as an impinging shock wave. In this case, a composite surface-pressure field (or a perturbed surface-pressure field) on a surface is given by
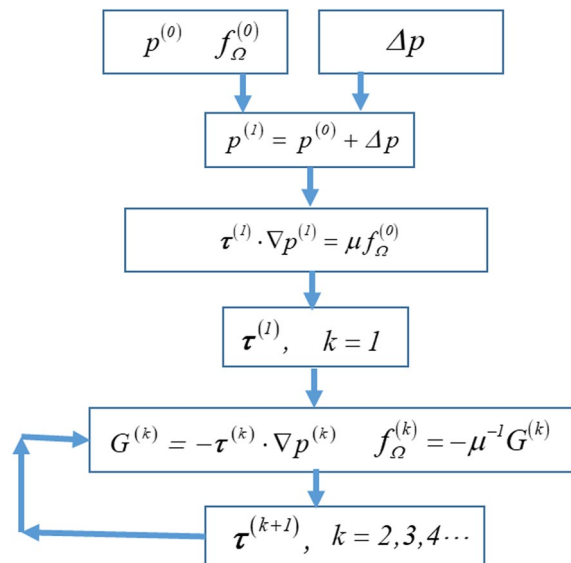
Fig. 1 Flowchart of the iterative approximate method

$$p^{(1)} = p^{(0)} + \Delta p, \tag{6}$$

where Δp is a surface-pressure variation. Therefore, the first-order $\boldsymbol{\tau}$-field denoted by $\boldsymbol{\tau}^{(1)}$ can be described by the first-order approximate equation $\boldsymbol{\tau}^{(1)} \cdot \nabla p^{(1)} = \mu f_\Omega^{(0)}$, where $f_\Omega^{(0)}$ is the base-flow BEF. Therefore, a $\boldsymbol{\tau}^{(1)}$-field can be obtained by solving the Euler–Lagrange equation, Eq. (4), with $G = G^{(0)} = -\mu f_\Omega^{(0)}$ that is known for the base flow. A heuristic iteration scheme is $G^{(k)} = -\boldsymbol{\tau}^{(k)} \cdot \nabla p^{(k)}$ $(k = 1, 2, \cdots)$ for iterative improvement in successive higher-order approximations, and accordingly the BEF is given iteratively by $f_\Omega^{(k)} = -\mu^{-1} G^{(k)}$.

In the first-order approximation, the base-flow BEF $f_\Omega^{(0)}$ is not affected in a short time. The underlying assumption is that the process of establishing a Δp-field is much faster than that of establishing a f_Ω-field. Since pressure is a result of molecule collisions in an equilibrium state, the characteristic timescale of establishing a Δp-field is $t_p \sim l/a_s$, where l is a length scale of a body and a_s is the speed of sound in fluid. In contrast, the physical mechanism of building a f_Ω-field is a viscous diffusion, which has a characteristic timescale $t_\Omega \sim \delta^2/\nu$, where δ is a viscous diffusion distance. An estimated ratio of the timescales t_p and t_Ω is $t_p/t_\Omega \sim M_{\mathrm{ref}}/Re_l^{1-2/n}$ [31], where M_{ref} is the local Mach number based on the near-wall velocity scale, and Re_l is the Reynolds number based on a body length scale l and n is an empirical exponent ($n \geq 2$). Therefore, since $t_p/t_\Omega \ll 1$ for $M_{\mathrm{ref}} \ll 1$ near the wall, the underlying approximation is plausible in a short time.

Essentially, the approximate method provides a practical alternative where the BEF of a known base flow is used in computation. Thus, a solution obtained by the approximate method gives a skin friction field induced by a surface pressure variation imposed on the base flow. This approach is applicable to the cases where the skin friction topology is dominated by the pressure gradient. Particularly, shock-wave/boundary-layer interaction (SWBLI) is such a case where an incoming boundary layer is used as the base flow and a measured surface pressure variation generated by a shock provides the surface pressure variation required for computation.

2.4 Base flow

A boundary layer could be selected as a base flow, where $\tau^{(0)}$, $p^{(0)}$ and f_Ω are expressed as the power-law functions of the surface coordinate in the main stream direction such that $\tau^{(0)} \cdot \nabla p^{(0)} = \mu f_\Omega^{(0)}$ is satisfied. The base-flow surface pressure and its gradient are given by

$$p^0 = c_0 + (c_1/2m)(x - x_0)^{2m}, \ \partial p^{(0)}/\partial x = c_1(x - x_0)^{2m-1}, \tag{7}$$

where c_0 and c_1 are proportional coefficients, x_0 is the virtual origin of the boundary layer, and m is a power-law exponent. Accordingly, skin friction and the BEF are given in the power-law relations, i.e.,

$$\tau^{(0)} = c_2(x - x_0)^{(3m-1)/2}, f_\Omega^{(0)} = c_3(x - x_0)^{(7m-3)/2}, \tag{8}$$

where c_2 and c_3 are proportional coefficients. The base flow with the power-law distributions of surface pressure, skin friction and BEF serves as a local approximation in many applications. The parameters m and x_0 can be determined by fitting surface pressure data obtained in measurements and computations before a surface pressure variation is imposed.

A theoretical base flow is the Falkner-Skan flow (the wedge flow) where the external velocity is $U(x) = ax^m$ [38, 39]. The boundary-layer velocity profile is given by $u(x,y)/U(x) = f(\eta)$, where $f(\eta)$ is the similarity function with the similarity variable η, where a is a positive constant and the wedge angle is given by $\pi\beta$ with $\beta = 2m/(m+1)$. The proportional coefficients are

$$c_1 = -\rho a^2 m, \ c_2 = \sqrt{(m+1)/2}\rho \nu^{1/2} a^{3/2} f''(0),$$

$$c_3 = -\mu\beta[a(m+1)/2\nu]^{3/2}a^2 f''(0),$$

where ν is the kinematic viscosity. The value of the second derivative f'' at the wall is approximately expressed as the piecewise functions extracted based on its tabulated numerical data [38].

$$f''(0) = 0.749m^{0.5049} + 0.4696, \ (0 \le m \le 1),$$

$$f''(0) = 1.696m + 0.4741, \ (-0.06 \le m \le 0.2).$$

2.5 Taylor-series-expansion solution

To reconstruct a near-wall velocity field, a Taylor-series-expansion solution near a solid surface (wall) in an incompressible viscous flow can be sought from the NS equations,

$$\rho\left(\frac{\partial \boldsymbol{u}}{\partial t} + \boldsymbol{u} \cdot \nabla \boldsymbol{u}\right) = -\nabla p + \mu\nabla^2 \boldsymbol{u}, \tag{9}$$

where $\boldsymbol{u}$ is the velocity, ρ is the fluid density, p is the pressure, and μ is the dynamic viscosity of fluid. The coefficients in the series-expansion solution are constrained by the NS equations and the continuity equation with the no-slip boundary condition [21, 22,

24]. This Taylor-series-expansion solution of the NS equations allows reconstruction of typical near-wall flow structures observed in 3D separated flows and wall-bounded turbulence [22, 24, 31].

When the $\boldsymbol{\tau}$- and p-fields in a viscous flow are known, the corresponding velocity field near a wall can be reconstructed by using the Taylor-series expansion solution of the NS equations [22, 31]. Consider the non-dimensional skin-friction $\overline{\boldsymbol{\tau}} = \boldsymbol{\tau}/\rho u_{\text{ref}}^2$ and surface-pressure $\overline{p} = p/\rho u_{\text{ref}}^2$, where u_{ref} is a reference velocity and the overhead bar denotes the non-dimensional quantities. For an incompressible viscous flow, the non-dimensional velocity vector normalized by u_{ref} parallel to the surface, which is denoted by $\overline{\boldsymbol{u}}_\pi = (\overline{u}_1, \overline{u}_2)$, is given by the Taylor-series expansion solution of the NS equations in the wall-normal coordinate, i.e.,

$$\overline{\boldsymbol{u}}_\pi = Re_l\left[\overline{x}_3\overline{\boldsymbol{\tau}} + \frac{\overline{x}_3^2}{2}\nabla p + \frac{\overline{x}_3^3}{6}(L\overline{\boldsymbol{\tau}} - \nabla(\nabla \cdot \overline{\boldsymbol{\tau}}))\right] + O\left(\overline{X}_3^4\right), \tag{10}$$

and the non-dimensional wall-normal velocity is

$$\overline{u}_3 = Re_l\left[-\frac{\overline{x}_3^2}{2}\nabla \cdot \overline{\boldsymbol{\tau}} - \frac{\overline{x}_3^3}{6}\nabla^2\overline{p}\right] + O\left(\overline{X}_3^4\right), \tag{11}$$

where $\overline{x}_3$ is the vertical coordinate normalized by a length scale l, $\overline{x}_i$ ($i = 1, 2$) are the normalized surface coordinates, $\nabla \equiv \nabla_s = (\partial/\partial\overline{x}_1, \partial/\partial\overline{x}_2)$ is the non-dimensional gradient operator on the surface, $L = (l^2/\nu)\partial/\partial t - \nabla^2$ is a non-dimensional differential operator, $Re_l = l\rho u_{\text{ref}}/\mu$ is the Reynolds number, and ν is the kinematic viscosity of fluid. The coefficients in the higher-order terms in Eqs. (10) and (11) are also functions of $\boldsymbol{\tau}$ and p [21].

In a region where the flow is attached, the velocity is dominated by the linear component, i.e., $\overline{\boldsymbol{u}}_\pi \approx Re_l\overline{x}_3\overline{\boldsymbol{\tau}}$ in parallel to the surface, and the vertical velocity component is mainly affected by the quadratic term, i.e.,

$$\overline{u}_3 \approx -Re_l\overline{x}_3^2\nabla \cdot \overline{\boldsymbol{\tau}}/2, \tag{12}$$

which is directly proportional to the skin friction divergence. However, near an isolated critical point with $\boldsymbol{\tau} = 0$, the velocity $\overline{\boldsymbol{u}}_\pi \approx Re_l\overline{x}_3^2\nabla\overline{p}/2$ parallel to the surface is mainly caused by the surface pressure gradient, and relatively the vertical velocity u_3 becomes significant.

Further, there is an exact on-wall relation between the wall-normal pressure gradient and the skin friction divergence, i.e., [22]

$$\left[\frac{\partial p}{\partial x_3}\right]_{\partial B} = -\nabla \cdot \boldsymbol{\tau}. \tag{13}$$

Equation (12) indicates that the positive and negative normal pressure gradients on a surface ∂B correspond to a sink (or separation line) and a source (or attachment line) in a skin friction field, respectively. If skin friction lines diverge at a point (i.e., a skin friction source), then $[\partial p/\partial x_3]_{\partial B} < 0$, indicating a decrease of pressure in the wall-normal

direction. If skin friction lines converge at a point (i.e., a skin friction sink), then $[\partial p/\partial x_3]_{\partial B} > 0$, indicating an increase of pressure in the wall-normal direction. The skin friction sink and source are related to the instantaneous local velocity profile in complex flows, inducing the ejection or the sweep events in wall-bounded turbulence, respectively [22].

2.6 The Poincare-Bendixson index formula

The topological rules are useful to interpret skin friction patterns in 3D separated flows [1–6]. For a penetrable boundary in a skin friction field, Liu et al. [17] applied the Poincare-Bendixson index formula (the P-B formula in short) to various flow cases, which presents a conservation law between isolated critical points and boundary switch points. In simple notations, the P-B formula is expressed as

$$\#N - \#S = 1 + \left(\#Z^+ - \#Z^-\right)/2, \tag{14}$$

where $\#N$ and $\#S$ denote the numbers of nodes and saddles in a domain, respectively, and $\#Z^+$ and $\#Z^-$ denote the numbers of positive and negative switch points on the domain boundary, respectively. If there is a point Z on a boundary at which the neighboring inflow and outflow segments are divided, this point is called a switch point.

There are two types of switch points. Figure 2 illustrates nodes and saddles in a domain Ω and negative and positive switch points on the penetrable domain boundary $\partial\Omega$ with inflow and outflow segments. By following a skin friction line (or a streamline), if the vector in a sufficiently small neighborhood of Z moves inward first and then outward across a boundary, this switch point is negative, which is denoted by Z^-. Otherwise, a switch point is positive, which is denoted by Z^+, if the vector moves outward first and then inward across a boundary in a neighborhood of Z^+. When inflow and outflow across a closed boundary $\partial\Omega$ remains qualitatively invariant such that $\#Z^+ - \#Z^-$ is fixed in Eq. (14), this conservation law indicates that nodes and saddles enclosed by the boundary must occur or disappear in pairs, which is the case in closed flow separations. The classical results, such as the hairy sphere theorem [18, 19], the topological rule given by Hunt et al. [4] for junction flows, and Foss' collapsed sphere method [14, 15], can be derived from Eq. (14).
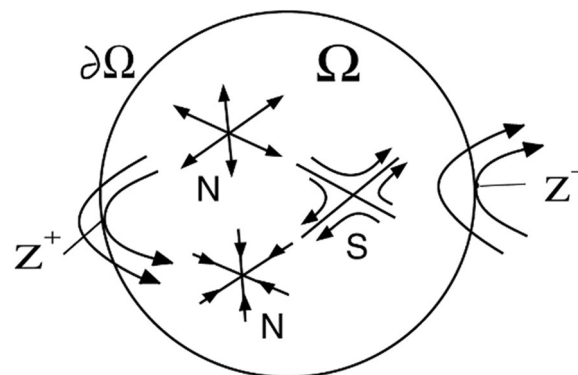

Fig. 2 Illustration of nodes, saddles, and positive and negative switch points. From Liu [26]

3 Elemental (τ, p)-structures

The important implication of the Taylor-series expansion solution of the NS equations, Eqs. (10) and (11), is that a near-wall velocity field is determined by the τ- and p-fields that are further constrained by the on-wall relation Eq. (1). Since τ and p are intrinsically coupled in a viscous flow, their structure on a surface is called the (τ, p)-structure here. From a theoretical perspective, reconstruction of the (τ, p)-structures is critical in order to understand near-wall viscous flows. Using the approximate method, Liu [31] reconstructed the elemental (τ, p)-structures (τ-source/sink and τ-vortex) and their combinations based on some simple forms of the surface-pressure variation imposed on the base flow with the power-law relations of the surface pressure, skin friction and BEF. In reconstruction of a τ-field by using the elemental (τ, p)-structures, the elemental Δp-structures and the $p^{(0)}$-field of the base flow are superposed linearly and then the corresponding $\tau^{(1)}$-field is obtained by using the approximate method based on the solution of the Euler–Lagrange equation. Apparently, the $\tau^{(1)}$-field reconstructed based on the τ-source/sink and τ-vortex is similar to a velocity field reconstructed by direct linear superposition of the elemental solutions (the uniform flow, source/sink and vortex) of the Laplace equation of the velocity potential in the classical potential flow theory. However, the important difference is that reconstruction of a $\tau^{(1)}$-field is a variational solution of the non-linear coupling (τ, p) relation (Eq. 1) that is a direct result of the NS equations applied to a solid surface in a viscous flow although the elemental Δp-structures are linearly superposed. Therefore, in this sense, the theoretical constructive method described in this paper is essentially of the non-linear nature.

3.1 Base flow

To evaluate the above approximate reconstruction method, the Falkner-Skan flow is used as a base flow in simulations, which has the non-dimensional external velocity distribution $U_e(x) = ax^m$, where x is the surface coordinate from the leading edge (normalized by a length scale l), the external velocity is normalized by u_{ref}, m is a power-law exponent, and a is a non-dimensional positive constant [38, 39]. The non-dimensional skin-friction and BEF distribution on the wedge surface is given based on the solution of the boundary-layer equation (see Section 2.4). In the following simulations, the Falkner-Skan flow with $a = 1$ and $m = 0.5$ is considered, which describes a boundary layer with a favorable constant pressure gradient on a wedge of the angle of $2\pi/3$). As an example, we use $\rho = 1\,\mathrm{kg \cdot m^{-3}}$, $u_{\mathrm{ref}} = 1\,\mathrm{m \cdot s^{-1}}$, $l = 1\,\mathrm{m}$, and $\nu = 1.5 \times 10^{-5}\,\mathrm{m^2 \cdot s^{-1}}$, $Re_l = u_{\mathrm{ref}}l/\nu$, and $p_0 = \rho u_{\mathrm{ref}}^2/2$. The non-dimensional results are not affected by the units. The coordinates are in the range of [0, 1] in meters, and the surface plane has 1000×1000 grid points (or pixels in the image plane). At the reference location of $x = 0.5$, the distance between two neighboring grid points corresponds to 3.5 viscous length units, where the viscous length unit is given by ν/u_τ with the friction velocity $u_\tau = \sqrt{\tau^{(0)}/\rho}$.

3.2 Skin friction source/sink

To reconstruct the elemental (τ, p)-structures, some simple forms of Δp are considered. The first idealized form of Δp is given by a Gaussian function, i.e.,

$$\Delta p = g_0 exp\left(-r^2/2\sigma^2\right), \tag{15}$$

where g_0 is the strength, the standard deviation σ defines the influential region, and the radial distance from the pressure center (x_c, y_c) is

$$r = \left[(x - x_c)^2 + (y - y_c)^2\right]^{1/2}.$$

Equation (15) describes a local high-pressure region for $g_0 > 0$ or a local low-pressure region for $g_0 < 0$. The $\boldsymbol{\tau}^{(1)}$-field is calculated when the Falkner-Skan flow is perturbed by the surface pressure variation, i.e., $p^{(1)} = p^{(0)} + \Delta p$, where $p^{(0)}$ is the Falkner-Skan flow pressure field. The $f_\Omega^{(0)}$- and $p^{(0)}$-fields (images) are generated. Then, the corresponding $\boldsymbol{\tau}^{(1)}$-field is obtained by solving the Euler–Lagrange equation. Since this method is designed for image processing, the figures of the fields in this section are shown in the image plane (x, y) in pixels. In the simulations, the standard deviation in Eq. (15) is $\sigma = 50$ pixels (grid points), which approximately corresponds to 175 viscous length units (ν/u_τ). The Δp-fields with the Gaussian distributions can be linearly superposed to reconstruct a synthetic complex $p^{(1)}$-field, and then the corresponding $\boldsymbol{\tau}^{(1)}$-field and near-wall velocity field can be obtained.

For a source-sink combination associated with the Gaussian Δp-distributions with $g_0 = \pm 0.2$ at the upstream and downstream locations, the $p^{(1)}$-field with the iso-pressure lines and the $\boldsymbol{\tau}^{(1)}$-field are shown in Figs. 3a and b, respectively. When the base flow is perturbed by a local high-pressure variation with $g_0 > 0$, the extracted $\boldsymbol{\tau}$-lines indicate a $\boldsymbol{\tau}$-source, as shown in Fig. 3b. In contrast, in a local low-pressure variation with $g_0 < 0$, a local low-pressure variation leads to a $\boldsymbol{\tau}$-sink, as also shown in Fig. 3b. The $\boldsymbol{\tau}$-source and $\boldsymbol{\tau}$-sink appear as the nodes N_1 and N_2 in the $\boldsymbol{\tau}^{(1)}$-field, respectively, while the two saddles (S_1 and S_2) are created along with the nodes. Further, the source node N_1 and sink node N_2 have the positive and negative skin friction divergence ($\nabla \cdot \boldsymbol{\tau}$), respectively. According to Eq. (13), N_1 and N_2 correspond to $[\partial p/\partial x_3]_{\partial B} < 0$ and $[\partial p/\partial x_3]_{\partial B} > 0$, respectively. This is consistent with the local high- and low-pressure regions at N_1 and N_2.

The distribution of the critical points obeys the topological constraint given by the P-B formula on a surface vector field (see Section 2.6) [17]. In this case where the $\boldsymbol{\tau}$-vectors in the far field are generally in the main stream direction, the topological rule for the critical points enclosed by a sufficiently large closed boundary on a surface is reduced to a simple form, i.e.,

$$\#N - \#S = 0,$$

where #N and #S denote the numbers of nodes and saddles, respectively. It is indicated that nodes and saddles in a $\boldsymbol{\tau}$-field occur or disappear in pairs in this flow. Indeed, the $(\boldsymbol{\tau}, p)$-structure in Fig. 3b (also in other figures in this section) satisfies this topological constraint, where the nodes and saddles are marked.

This $(\boldsymbol{\tau}, p)$-structure with a source-sink combination corresponds to a closed 3D flow separation pattern. In addition to the critical points, separation and attachment lines (denoted by SL and AL hereafter) are the distinct topological features in a $\boldsymbol{\tau}$-field in complex separated flows. Here, a SL is defined as a $\boldsymbol{\tau}$-line to which all neighboring $\boldsymbol{\tau}$
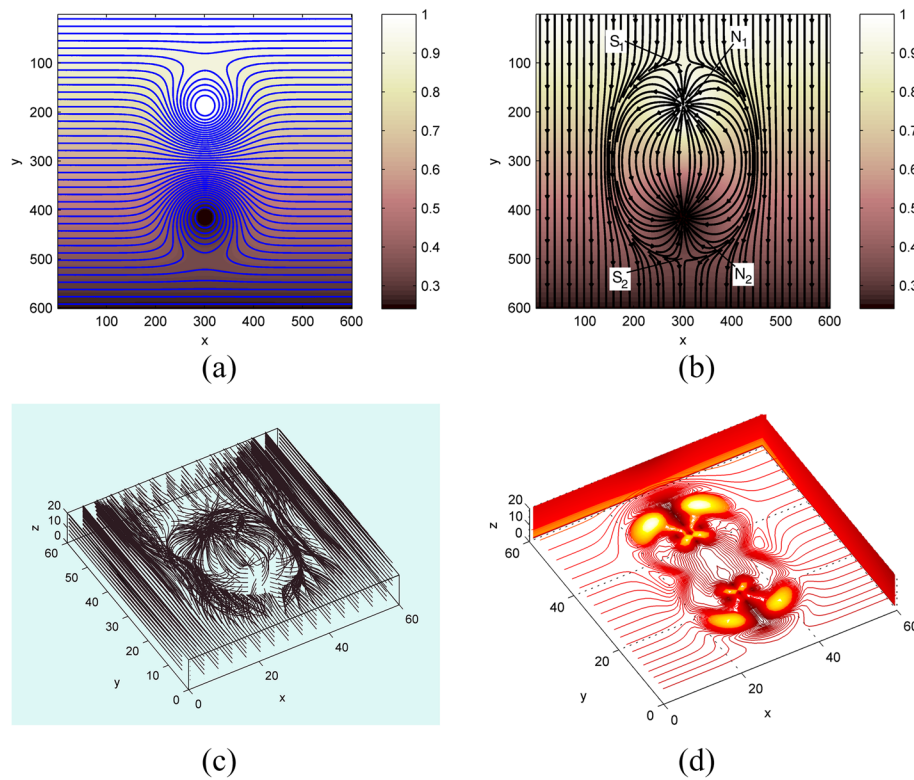
Fig. 3 Source-sink structure in a $\boldsymbol{\tau}^{(1)}$-field: **a** the normalized $p^{(1)}$-field with iso-pressure lines, **b** $\boldsymbol{\tau}$-lines overlaid on the $p^{(1)}$-field, **c** near-wall streamlines, and **d** contours of the enstrophy near a wall. The freestream flow is aligned with the *y*-direction in the image plane. From Liu [31]

-lines converge and accumulate asymptotically. Similarly, an AL is a $\boldsymbol{\tau}$-line from which all neighboring $\boldsymbol{\tau}$-lines are originated and diverged. As shown in Fig. 3b, the envelope enclosing the separation region can be segmented into the front part and the back part. The front segment is the SL originated from the front saddle S_1 and the back segment is the AL connecting to the rear saddle S_2. This $(\boldsymbol{\tau}, p)$-structure can be found in a viscous flow over the surface of a tandem pair of a valley (with $\Delta p > 0$) high and a bump (with $\Delta p < 0$), and the $\boldsymbol{\tau}$-topology in Fig. 3b is consistent with that obtained in the numerical simulations of the flows over local deformed surfaces [40].

The reconstructed near-wall streamlines and contours of the enstrophy near the wall are shown in Fig. 3c and d, respectively, where the spatial resolution is downsampled by 10 for clear illustration. Near the $\boldsymbol{\tau}$-source, the wall-normal velocity points into the wall due to the positive skin friction divergence $\nabla \cdot \boldsymbol{\tau} > 0$ $\left([\partial p/\partial x_3]_{\partial B} < 0\right)$. In other words, the local positive Δp-distribution leads to the negative wall-normal velocity near the $\boldsymbol{\tau}$-source. In contrast, near the $\boldsymbol{\tau}$-sink with the local negative Δp-distribution, the positive wall-normal velocity pointing outward from the wall (fluid upwelling) is generated due to the negative skin friction divergence $\nabla \cdot \boldsymbol{\tau} < 0$ $\left([\partial p/\partial x_3]_{\partial B} > 0\right)$. In general, the wall-normal velocity magnitude near the critical points and SL/AL is significantly larger than that in other regions. Interestingly, this relationship between the surface pressure variation and the wall-normal velocity near the nodes is consistent with the

observations of the phenomena of intermittent and localized backflows and wall-normal flows in near-wall turbulence [41–43]. The backflows with negative skin friction generally occur in some neighboring regions of the critical points in the $(\boldsymbol{\tau}, p)$-structures. In addition, the 3D concentrated enstrophy features near the wall are generated around the critical points. The critical points in these $(\boldsymbol{\tau}, p)$-structures signify local flow separations although the mean flow is not separated.

3.3 Skin friction vortex

Another simple form of Δp is a helical surface-pressure variation given by

$$\Delta p = \gamma_0 \arctan(\theta), \tag{16}$$

where γ_0 is the strength and θ is the polar angle.

$$\theta = \tan^{-1}\big[(y - y_c)/(x - x_c)\big].$$

It is found that it generates a counter-clockwise $\boldsymbol{\tau}$-vortex imbedded in the base flow. Figures 4a and b show the $p^{(1)}$-field with the iso-pressure lines and the $\boldsymbol{\tau}^{(1)}$-field for $\gamma_0 = -0.2$. As shown in Fig. 4b, the $\boldsymbol{\tau}$-vortex (the node N_1) induces a saddle S_1, which naturally meets the topological constraint given by the P-B formula. Figure 4c and d show the near-wall streamlines and contours of the enstrophy near a wall, respectively. The SL is formed partially in the upstream of the $\boldsymbol{\tau}$-vortex, while the AL appears partially in the downstream. This $(\boldsymbol{\tau}, p)$-structure with a vortex-saddle combination could result from the interaction between a tornado-like-vortex and a boundary layer. This vortex-saddle structure has been observed in near-wall turbulence [40].

Further, a $\boldsymbol{\tau}$-vortex pair is reconstructed as a typical structure observed in the 3D separated flow over a low-aspect-ratio rectangular wing and the flow behind a junction [17, 23]. Figure 5 shows the reconstructed flow fields associated with a $\boldsymbol{\tau}$-vortex pair with $\gamma_0 = \pm 0.2$, where the vortex pair is marked as the nodes N_1 and N_2 while the saddles S_1 and S_2 appear upstream and downstream, respectively. This $(\boldsymbol{\tau}, p)$-structure represents another type of closed flow separations, where the front segment of the envelope is the SL originated from the front saddle S_1, and the back segment of the envelope is the AL connecting to the rear saddle S_2.

It is known that a $\boldsymbol{\tau}$-vortex pair is a building block to reconstruct the complex separated flow over a topographic hill model. To simulate this flow, the Δp-field associated with two $\boldsymbol{\tau}$-sinks with $g_0 = -0.2$ is superposed at the centers of the $\boldsymbol{\tau}$-vortex pair to generate the low-pressure regions there. Then, the Δp-field associated with a $\boldsymbol{\tau}$-source with $g_0 = 0.2$ is added upstream of the $\boldsymbol{\tau}$-vortex pair. Figure 6 shows the $p^{(1)}$-field, $\boldsymbol{\tau}^{(1)}$-field, near-wall streamlines and contours of the enstrophy near the wall in this flow. This $(\boldsymbol{\tau}, p)$-structure corresponds to the observed separated flow over a generic topographic hill model [44], and particularly the pattern around the $\boldsymbol{\tau}$-vortex pair is called the owl-face of the first kind [20, 45]. The streamlines near the vortex centers spiral upward due to the presence of the low-pressure regions.
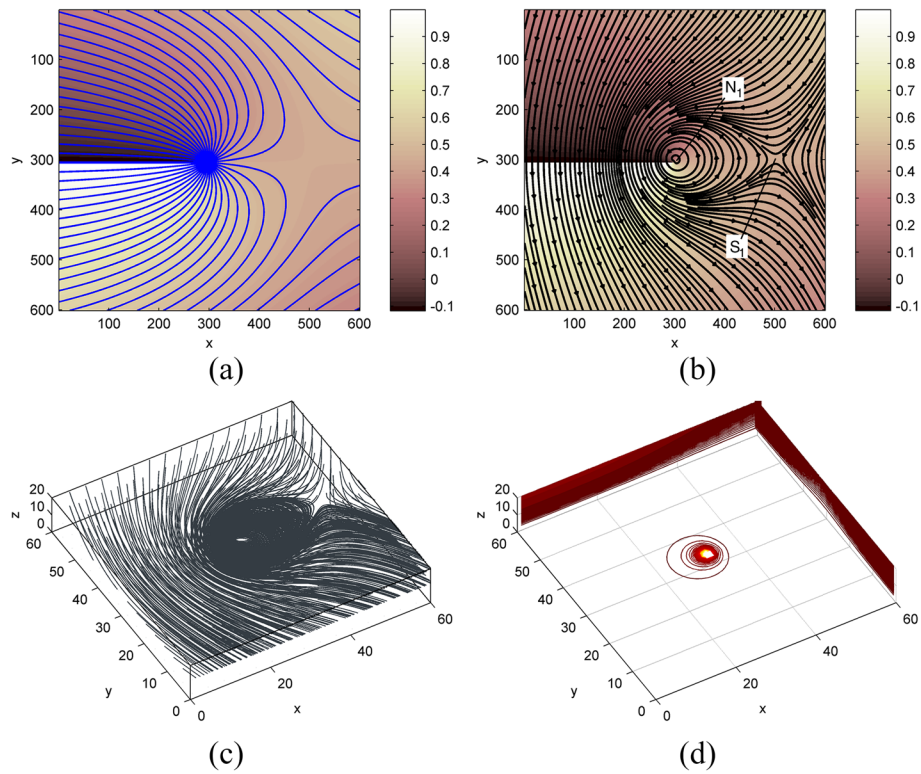
Fig. 4 Vortex structure in a $\boldsymbol{\tau}^{(1)}$-field: **a** the normalized $p^{(1)}$-field with iso-pressure lines, **b** $\boldsymbol{\tau}$-lines overlaid on the $p^{(1)}$-field, **c** near-wall streamlines, and **d** contours of the enstrophy near a wall. The freestream flow is aligned with the *y*-direction in the image plane. From Liu [31]

4 Complex (τ, p)-structures

4.1 Swept SWBLI

It is conjectured that the formation of the SL and AL in complex separated flows could be associated with distinct continuously-distributed features in a Δp-field [31]. To examine this conjecture, the rapid change of Δp across a curve on a surface is considered, which could be caused by swept shock-wave/boundary-layer interaction (SWBLI). To simulate this flow, across a shock wave located at a curve described by a parametric equation $[x_c(s), y_c(s)]$ with the arc length s, the surface-pressure variation across the shock wave is given by

$$\Delta p = g_0[1 + \tanh{(n/h)}], \tag{17}$$

where n is the normal coordinate on the curve (the shock wave location) and h a parameter associated with the surface pressure variation width associated with the shock wave. Here, a straight swept shock wave interacting with the Falkner-Skan flow is considered.

The $p^{(1)}$-field generated by a straight 45°-swept shock with $g_0 = 0.1$ on the base flow and the $\boldsymbol{\tau}$-lines reconstructed from the $p^{(1)}$-field are shown in Figs. 7a and b, respectively. The near-wall streamlines and contours of the enstrophy near the wall are shown in Fig. 7c and d, respectively. Clearly, the SL occurs immediately upstream of the pressure jump associated with the shock wave, and the AL appears after the shock wave. This
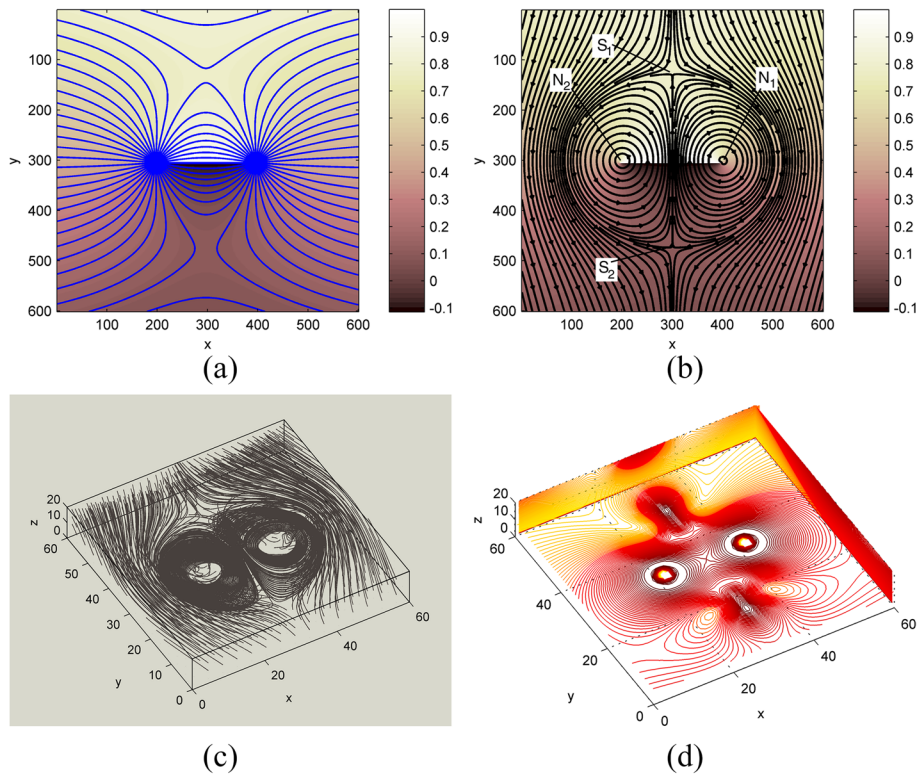
Fig. 5 Vortex-pair structure in a $\boldsymbol{\tau}^{(1)}$-field: **a** the normalized $p^{(1)}$-field with iso-pressure lines, **b** $\boldsymbol{\tau}$-lines overlaid on the $p^{(1)}$-field, **c** near-wall streamlines, and **d** contours of the enstrophy near a wall. The freestream flow is aligned with the *y*-direction in the image plane. From Liu [31]

$(\boldsymbol{\tau}, p)$-structure corresponds to a 3D separation bubble observed in shock-wave/boundary-layer interaction (SWBLI) on a transonic swept wing [46].

4.2 Fin-induced SWBLI

In a supersonic flow, a swept shock wave generated by a sharp fin vertically mounted on a flat floor interacts with the floor boundary layer (BL). The flow structures in this typical SWBLI have been extensively studied [46–49]. The incoming BL separates upstream of the inviscid shock wave and the flow re-attaches near the fin surface. As a result, a conical (or quasi-conical) separation bubble is formed, and the normalized distributions of the surface pressure and heat transfer along the circular arcs are approximately independent from the radial coordinate from the virtual origin of the shock wave [49]. The secondary separation and re-attachment may exist, depending on the strength of the shock wave and the conditions of the incoming boundary layer. The skin-friction topological structures in the fin-induced SWBLIs are usually inferred based on surface oil-steak visualizations.

To simulate this flow, the conical distribution of the surface pressure variation in a polar coordinate system is given by

$$\Delta p = g_0[1 + \tanh ((\theta - \theta_s)/\Delta\theta)], \tag{18}$$
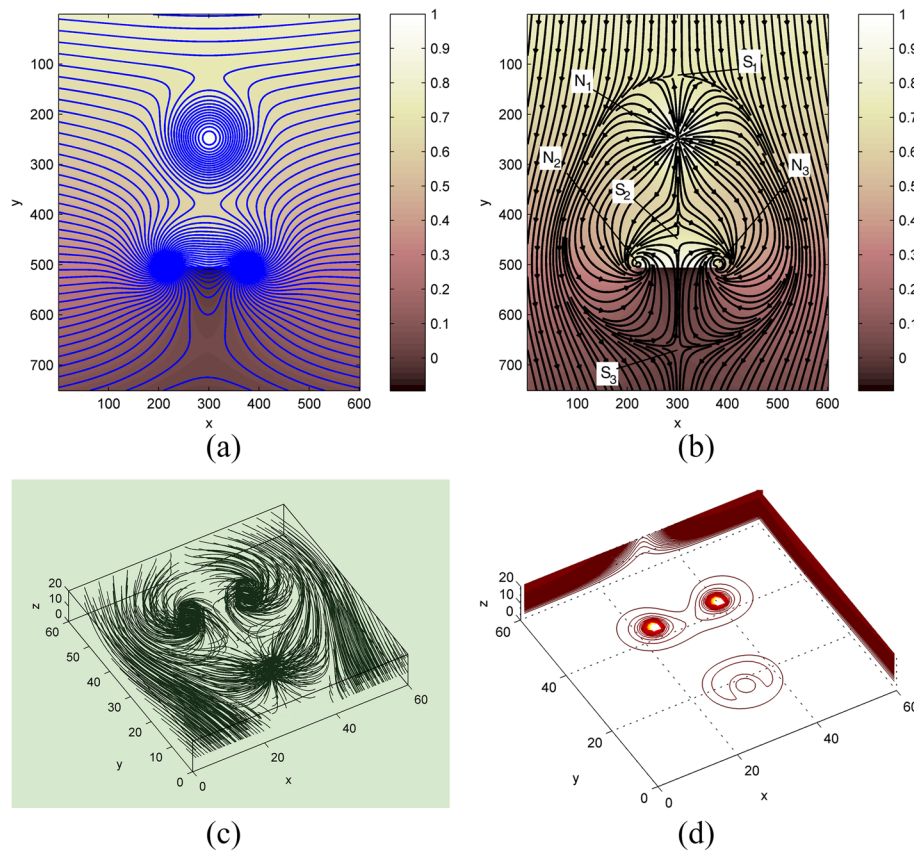
Fig. 6 Hill model structure in a $\boldsymbol{\tau}^{(1)}$-field: **a** the normalized $p^{(1)}$-field with iso-pressure lines, **b** $\boldsymbol{\tau}$-lines overlaid on the $p^{(1)}$-field, **c** near-wall streamlines, and **d** contours of the enstrophy near a wall. The freestream flow is aligned with the *y*-direction in the image plane. From Liu [31]

where θ is the polar angle of a ray from the x-coordinate (the horizontal axis in the image plane, as shown in Fig. 8a, θ_s is the polar location of the inviscid shock wave, and $\Delta\theta$ is a parameter that describes the angular width of the surface pressure variation associated with shock wave. The synthetic surface pressure field $p^{(1)} = p^{(0)} + \Delta p$ is obtained by superposing the Δp-field on the $p^{(0)}$-field for $g_0 = 0.1$, $\theta_s = 60°$ and $\Delta\theta = 5°$. In this case, the fin surface is located at $\theta = 80°$, the fin wedge angle is $10°$, the shock angle is $40°$, and the incoming freestream Mach number is 1.97.

Figures 8a and b show the $p^{(1)}$-field and the extracted $\boldsymbol{\tau}$-lines in the fin-induced SWBLI, respectively. The SL forms immediately upstream of the shock wave approximately at $\theta = 50°$, and the AL occurs approximately at $\theta = 70°$ near the fin surface. This $(\boldsymbol{\tau}, p)$-structure, along with the primary topological features, is qualitatively consistent with the previous observations [46, 47]. The near-wall streamlines and contours of the enstrophy near the wall are shown in Fig. 8c and d, respectively.

4.3 Delta wing

The $(\boldsymbol{\tau}, p)$-structures in the flow over a delta wing are associated with the leading-edge vortices. A hypothetical situation is considered to simulate the flow over a delta wing. It is assumed that the base flow over the upper surface of a delta wing is attached initially,
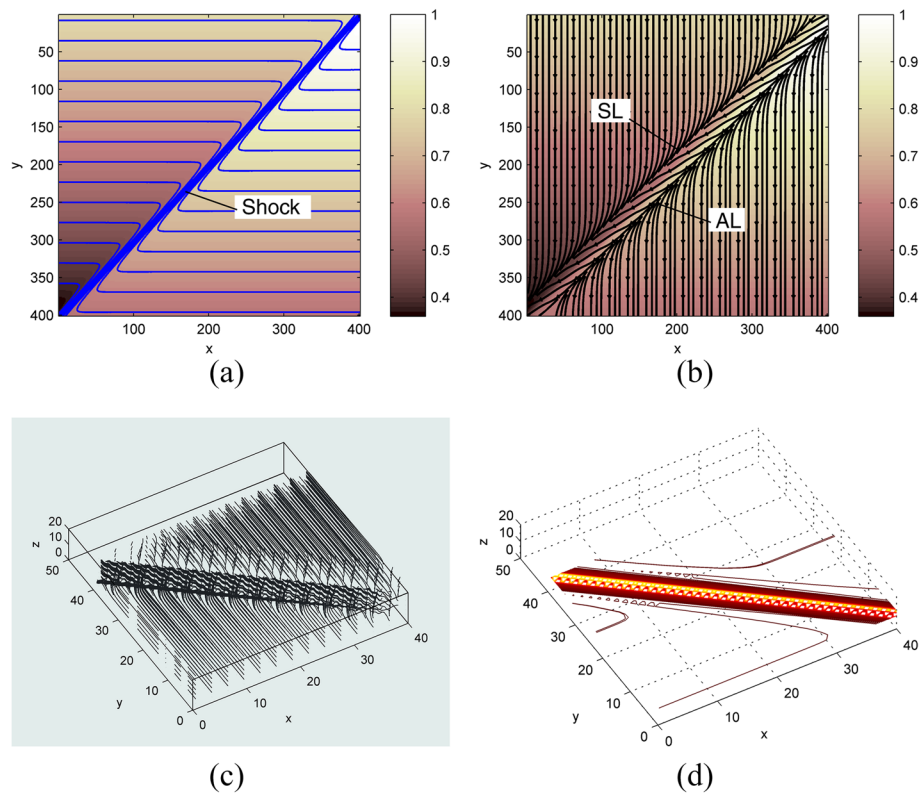
Fig. 7 Swept-shock structure in a $\boldsymbol{\tau}^{(1)}$-field: **a** the normalized $p^{(1)}$-field with iso-pressure lines, **b** $\boldsymbol{\tau}$-lines overlaid on the $p^{(1)}$-field, **c** near-wall streamlines, and **d** contours of the enstrophy near a wall. The freestream flow is aligned with the *y*-direction in the image plane. From Liu [31]

and then a Δp-field associated with the leading-edge vortices is suddenly imposed on the base flow to form the separated flow observed in experiments. To investigate this problem, a 70°-delta wing is considered as a typical case at the angle of attack (AoA) of 20°, Mach number of 0.55 and total pressure of 100 kPa. The normalized surface pressure variation field obtained in CFD simulation [23] is superposed on the $p^{(0)}$-field for the base flow to reconstruct a synthetic surface-pressure field $p^{(1)} = p^{(0)} + \Delta p$. The $p^{(1)}$-field and the extracted $\boldsymbol{\tau}$-lines on the delta wing are shown in Figs. 9a and b, respectively. The separation lines are located approximately at the ray lines of 75.7° and 104.3° swept angles near the leading edges, while the attachment line is at the centerline of the delta wing. This $\boldsymbol{\tau}$-topology on the delta wing is consistent with the CFD result [23]. The near-wall streamlines and contours of the enstrophy near the wall are shown in Fig. 9c and d, respectively.

5 Applications in experiments

5.1 Incident SWBLI

To obtain high-resolution $\boldsymbol{\tau}$-fields in experiments, the approximate method was applied by Liu et al. [32] to unsteady pressure sensitive paint (PSP) images obtained in incident SWBLIs at Mach 2.5 for different Reynolds numbers, revealing the skin friction structures of the flows, particularly the separation bubble induced by the incident shock
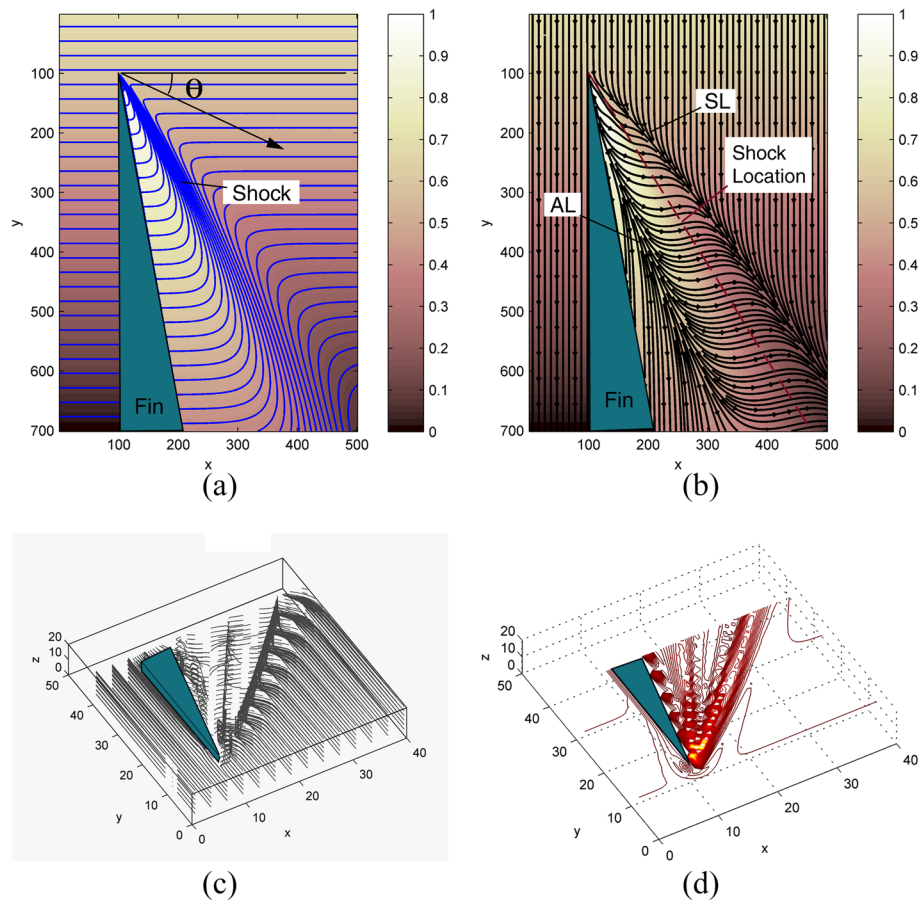
Fig. 8 Fin-induced shock-wave/boundary-layer interaction: **a** the normalized $p^{(1)}$-field with iso-pressure lines, **b** τ-lines overlaid on the $p^{(1)}$-field, **c** near-wall streamlines, and **d** contours of the enstrophy near a wall. The freestream flow is aligned with the *y*-direction in the image plane. From Liu [31]

wave. Unsteady PSP measurements in incident SWBLIs were conducted by Woike et al. [50] in the NASA Glenn Research Center 17-cm Axisymmetric Wind Tunnel (the 17-cm Axi-SWT). A shock generated by a 13.5° cylindrical cone impinges on the wall and interacts with the floor boundary layer at different total pressures and Reynolds numbers (Re_D) based on the test section diameter. Figure 10 shows the SWBLI region of interest in the Mach 2.5 Axisymmetric test section [50, 51], where the origin of the *x*-coordinate is set at the location of the maximum surface pressure gradient in the surface pressure rise induced by the impinging shock wave. Unsteady PSP measurements were made by using Innovative Scientific Solutions Inc. (ISSI) Turbo PSP with 2 kHz time response. PSP images were acquired at 4 kHz using the Photron SA-Z high-speed camera and then converted to surface pressure fields using the PSP calibration relation.

Figure 11 shows the time-averaged *p*-fields normalized by the atmospheric pressure ($p_{stm} = 1$ atm) at Mach 2.5, where the Reynolds numbers (Re_D) based on the test section diameter (17 cm) are 5, 4, 3, 2 and 1.5 million from the top to bottom, respectively. These fields are obtained by averaging sequences of 2000 fields. The coordinates are normalized by the boundary-layer thickness $\delta = 13.1$ mm measured at about 5 mm before the shock wave impingement [52]. The spanwise-averaged *p*-profiles are normalized
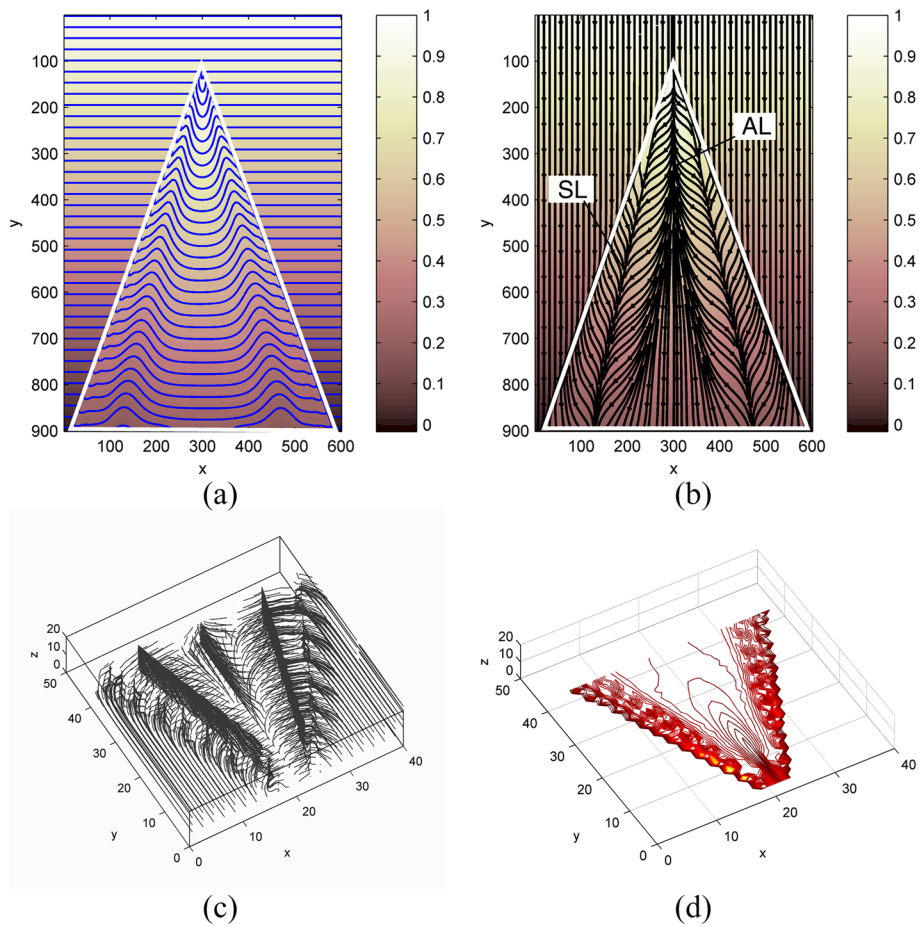
Fig. 9 The 70°-delta-wing at AoA of 20° and Mach number of 0.55: **a** the normalized $p^{(1)}$-field with iso-pressure lines, **b** τ-lines overlaid on the $p^{(1)}$-field, **c** near-wall streamlines, and **d** contours of the enstrophy near a wall. The freestream flow is aligned with the *y*-direction in the image plane. From Liu [31]
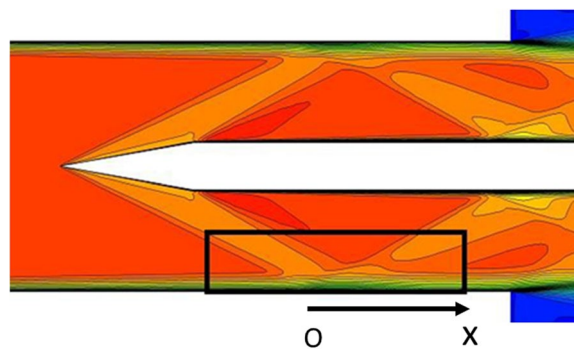
Fig. 10 SWBLI region of interest (marked by a rectangle) in the Mach 2.5 Axisymmetric test section. Flow is from left to right. From Liu et al. [32]

by the values at the location ($x = -65$ mm) upstream of the shock wave, as shown in Fig. 12. Here, the origin of the *x*-coordinate is set at the location where the maximum surface pressure gradient is attained at $Re_D = 5$ million. The surface pressure data in
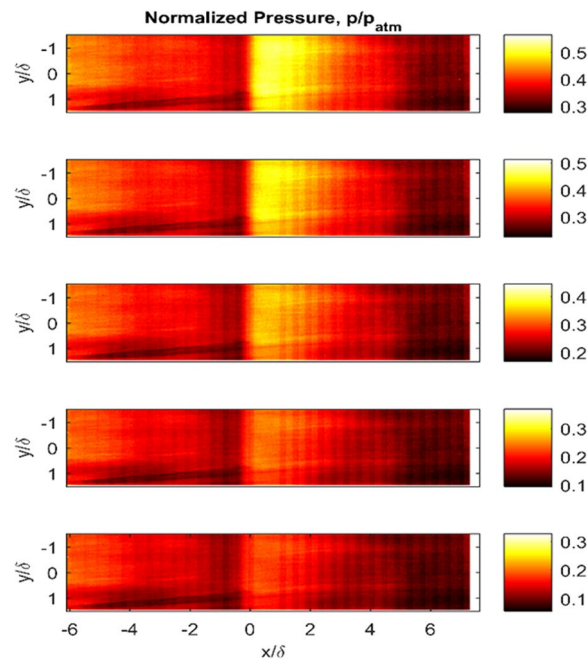
Fig. 11 Time-averaged surface pressure fields normalized by one atmospheric pressure at Mach 2.5 in incident SWBLI generated by a 13.5° cylindrical cone. From the top plot to bottom plot, the Reynolds numbers (Re_D) are 5, 4, 3, 2 and 1.5 million, respectively. Flow is from left to right. From Liu et al. [32]

the incoming boundary layer before the region of incident SWBLI is fitted by using the power-law relation

$$p(x)/p(x_{\text{ref}}) = 3.65 - (x - x_0)^{2m}, \tag{19}$$

where the virtual origin of the incoming boundary layer is $x_0 = -200$ mm, the reference location is $x_{\text{ref}} = -65$ mm and the power-law exponent is $m = 0.1$. This empirical power-law relation is used as the base-flow p-field for reconstruction of the τ-fields. The surface pressure increases rapidly to the peak immediately after a shock wave and then decays in a downstream region of 100 mm. The ratio between the PSP-measured surface pressures after and before a shock wave is $p_2/p_1 \approx 1.6 - 1.75$ in a range of Re_D from 1.5 to 5 million, which is consistent with the value of $p_2/p_1 \approx 1.7$ given by Davis [51] based on the pressure tap measurement.

The normalized τ-fields are extracted from the corresponding p-fields by using the approximate method. The incoming boundary layer is used as the base flow with the power-law distributions of surface pressure and BEF where the exponent is $m = 0.1$. The Lagrange multiplier is set at $\alpha = 10^{-5}$ in solving the Euler–Lagrange equation. Figure 13 shows the time-averaged p-fields normalized by its maximum value, τ-vectors, and τ-lines at Mach 2.5 for $Re_D = 5$ million. There are 230×420 vectors extracted in the regions of interest in Fig. 13, and the spatial resolution of the data is one vector per pixel. One pixel corresponds to 16 μm on the surface. The separation bubble induced by incident SWBLI occurs, where the separation and attachment lines are clearly identified in the skin friction topology in Fig. 13. Figure 14 shows the profiles of the x-component of skin friction normalized by the values at a reference location marked in Fig. 12 at Mach
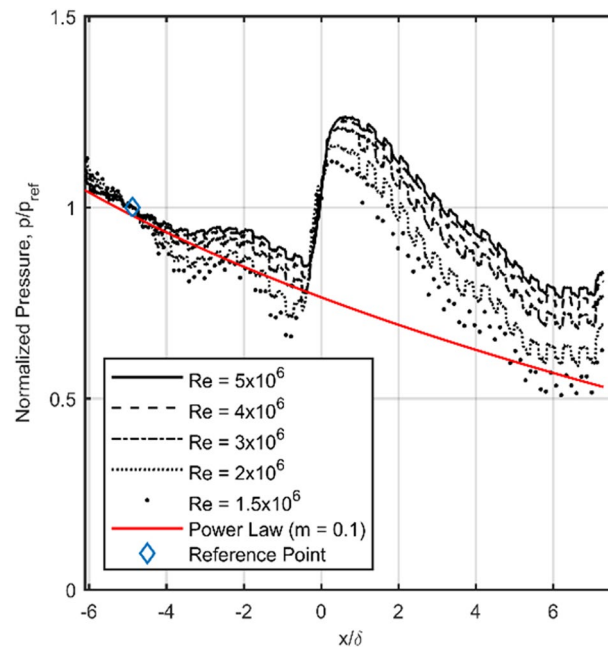
Fig. 12 Surface pressure profiles normalized by the values at a reference location marked in the figure for different Reynolds numbers (Re_D), and a power-law fitting of data for the incoming boundary layer. From Liu et al. [32]

2.5 for $Re_D = 4$, 3, 2, and 1.5 million. The extracted skin friction vectors and lines for these values of Re_D are similar to those in Fig. 13. The bubble length L_b is introduced as the distance between the separation line and the attachment line. An estimate based on the measurements is $L_b/\delta \approx 1$, which is consistent with CFD simulation [52].

Measurements with surface stress sensitive films (S3F) were made in incident SWBLIs generated by the 13.5° shock generator at Mach 2.5 at $Re_D = 1.5$ and 2 million [49]. Figure 15 shows comparisons between the results obtained by PSP and S3F in the region near the separation bubble for $Re_D = 2$ million. The τ-field obtained by S3F has 23×49 vectors in the region, in contrast to 231×476 vectors extracted from PSP images. The relative τ-fields obtained by PSP are anchored in in-situ calibration by using the S3F data (52 Pa for $Re_D = 2$ million) at the reference location $x = 20$ mm marked in Fig. 15. The separation bubble is detected by both PSP and S3F. The results obtained by PSP exhibit some 3D features, particularly the streamwise streaky structures after re-attachment. The spanwise-averaged profiles of the x-component of τ are shown in Fig. 16, indicating that the results extracted from PSP agree with the S3F data. This example indicates that the reconstruction method of a τ-field from a p-field is particularly attractive and applicable for high-resolution PSP measurements in complex flows (such as SWBLI) since PSP has been used as a non-contact global technique in various aerodynamics experiments [53].

5.2 Swept SWBLI

The approximate method was used by Liu et al. [33] to elucidate the relationship between the τ-topology of the secondary separation bubble and the p-field in the

Normalized Pressure
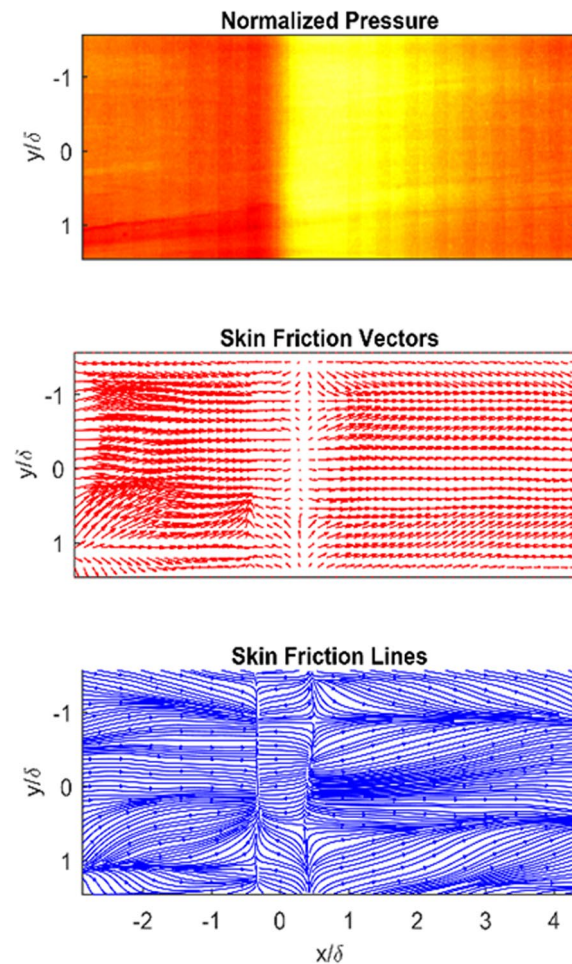
Skin Friction Vectors

Skin Friction Lines

Fig. 13 Time-averaged fields of the normalized surface pressure by its maximum value, extracted skin friction vectors and lines at Mach 2.5 for $Re_D = 5$ million. Flow is from left to right. From Liu et al. [32]

fin-generated SWBLI. The primary separation and attachment in swept SBLI constitute a large conical separation bubble [54–59]. Interestingly, the secondary separation in swept SWBLIs was observed in experiments and CFD simulations [54, 58] and its possible existence was discussed from a theoretical standpoint [59]. However, data on the secondary separation are very limited. From a topological perspective, the secondary separation should be described as the secondary separation bubble (SSB) with a pair of the separation and attachment lines. Here, the term 'separation bubble' is generalized to describe a separation flow confined in a conical space that is confined by the two sides and open at the end. To study the formation of the SSB, the evolution of the τ-topology extracted from a p-field in swept SWBLI is studied as the relevant parameters to a p-field vary.

The quasi-conical similarity of a p-field in swept SWBLIs was supported by surface pressure measurements along several radial arcs from the leading edge of the fin [49, 60]. PSP measurements in swept SWBLIs were conducted by Mears et al. [61] and Baldwin [62], providing the high-resolution p-fields to examine the conical similarity. Figure 17a shows the time-averaged p-field normalized by the incoming
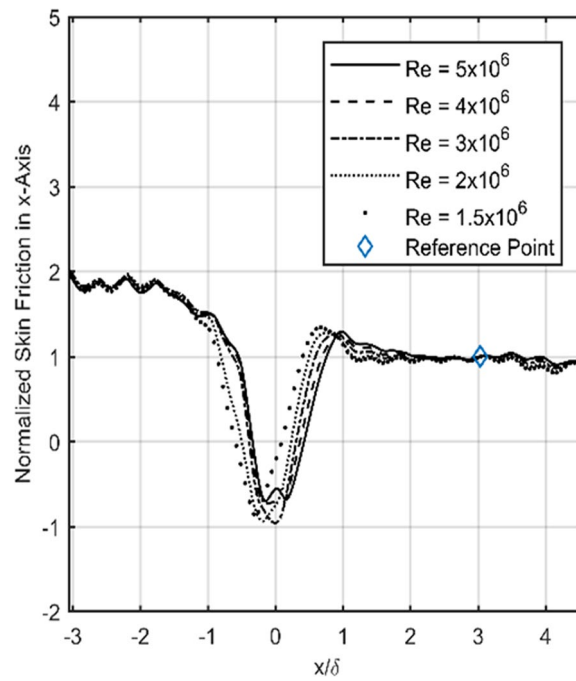
Fig. 14 Profiles of the *x*-component of skin friction normalized by the values at a reference location marked in Fig. 12 at Mach 2.5 for different Reynolds numbers (Re_D). From Liu et al. [32]
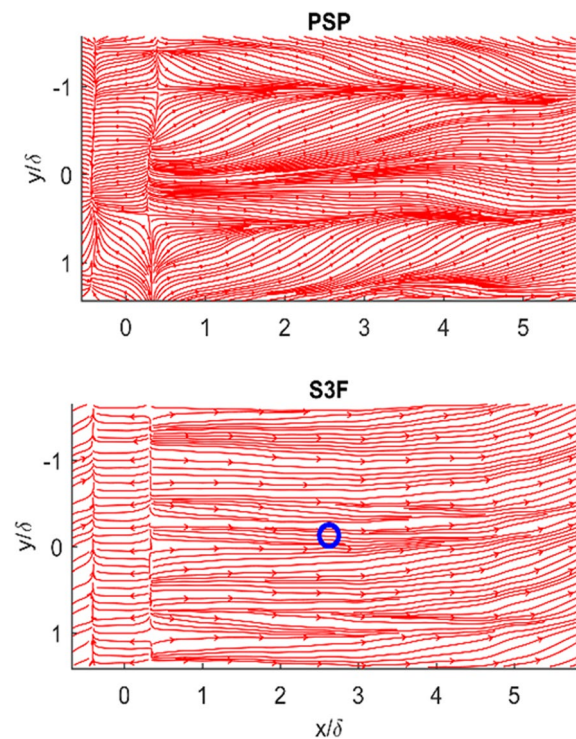

Fig. 15 Comparison between skin friction lines obtained by PSP and S3F for $Re_D = 2$ million, where the circle marks the reference location for in-situ calibration. Flow is from left to right. From Liu et al. [32]
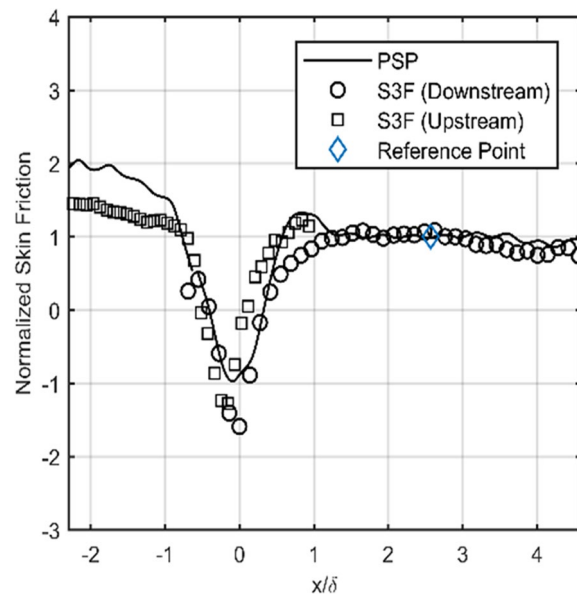
Fig. 16 Comparison between profiles of the *x*-component of skin friction obtained by PSP and S3F for $Re_D = 2$ million, where the diamond marks the reference location for in-situ calibration. From Liu et al. [32]

boundary layer pressure obtained from PSP measurements at Mach 2 with a fin deflection angle of 15° (Case 1) [61]. For simplicity, in an ideal case of inviscid flow, the (*x*, *z*) coordinate system is located at the apex of the fin (the floor/fin leading-edge junction), where *x* and *z* are the coordinates in the freestream and spanwise directions, respectively. When the flow structures in swept SWBLI exhibit the conical similarity approximately, the polar coordinate system (θ, r) is usually used, where θ is the polar angle and *r* is the radial coordinate. In reality, in swept SWBLIs, there is a so-called inception zone where the visualized surface quantities (pressure, temperature, heat flux, and skin friction) are not exactly conically similar and the relevant interaction footprints (such as separation line and surface pressure jump line) are curved [59, 60]. Only in the flow downstream beyond the inception zone, these surface quantities become asymptotically invariant along straight ray lines through the virtual conical origin (VCO) that can be determined as an intersection between the inviscid shock wave and the asymptotically straight primary separation line.

The normalized surface pressure $\Delta \bar{p} = (p - p_{\mathrm{ref}})/\max(p - p_{\mathrm{ref}})$ is evaluated along the radial arcs marked in Fig. 17a, where p_{ref} is the surface pressure (p_∞) in the incoming boundary layer before SWBLI. The profiles of $\Delta \bar{p}$ along the arcs are shown in Fig. 17b. It is indicated that the profiles (as a function of the polar angle) at different *r*-coordinates approximately collapse when *r* is larger than a critical length. This indicates that the conical similarity of surface pressure is asymptotically achieved as the radial coordinate *r* increases. The general trend of the profiles is that $\Delta \bar{p}$ increases with the polar angle θ and reaches the maximum near the fin surface. There is a plateau in the middle section of the *p*-curve, which has been observed in the previous measurements with distributed pressure taps [58, 59]. The relationship between the surface pressure plateau (*p*-plateau) and τ-structure is particularly relevant to the formation of the SSB.
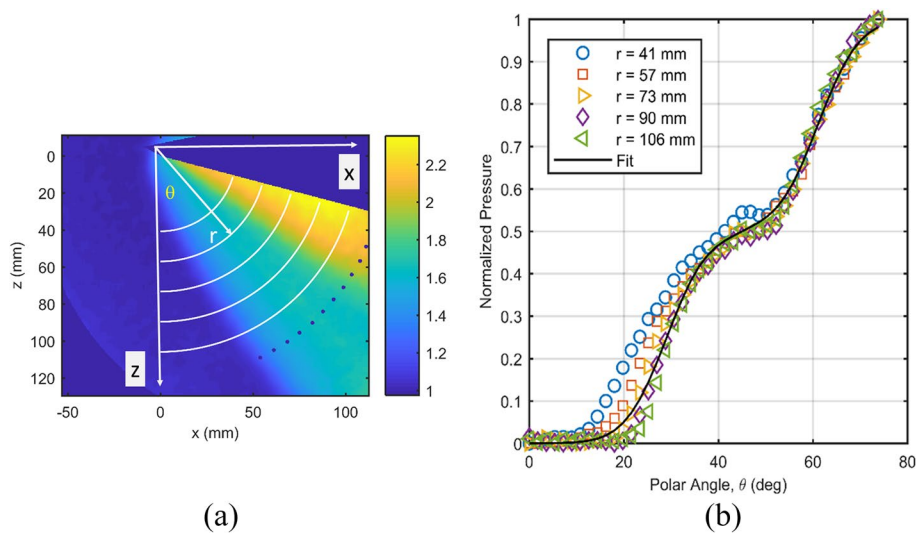
Fig. 17 PSP results in swept SWBLI at Mach 2 with a fin deflection angle of 15° [24]: **a** normalized surface pressure image by the incoming boundary layer pressure (p/p_∞), and **b** normalized surface pressure ($\Delta\bar{p}$) profiles at five radial arcs. From Liu et al. [33]

To describe the conically similar structure of surface pressure in swept SWBLI, Liu et al. [33] proposed the following empirical distribution to fit experimental surface pressure data, i.e.,

$$\Delta\bar{p}(\theta) = \frac{p - p_{\text{ref}}}{\max\,(p - p_{\text{ref}})} = \frac{1}{2}\left[1 + \tanh\left(\frac{\theta - \theta_s}{w_s}\right)\right] + g(\theta - \theta_s), \tag{20}$$

where

$$g(\theta - \theta_s) = \frac{a_{\text{pl},1}}{\sqrt{2\pi}\sigma}\exp\left[-\left(\frac{\theta - \theta_s + \Delta\theta_1}{\sqrt{2}\sigma}\right)^2\right] - \frac{a_{\text{pl},2}}{\sqrt{2\pi}\sigma}\exp\left[-\left(-\frac{\theta - \theta_s + \Delta\theta_2}{\sqrt{2}\sigma}\right)^2\right]. \tag{21}$$

In the RHS of Eq. (20), the first term describes a typical surface pressure change across a shock wave and the second term describes the p-plateau. The parameters θ_s and w_s define the angular location and influence width of a shock wave, respectively. The function $g(\theta - \theta_s)$ has positive and negative Gaussian peaks that are located on the left and right sides of a shock wave, respectively, where $\Delta\theta_i$ ($i = 1, 2$) defines a shift of a peak from the shock wave location θ_s, the standard deviation σ defines the width of a peak, and $a_{\text{pl},i}$ is the p-plateau amplitude ($i = 1$ or 2). In a special case with $\Delta\theta \equiv \Delta\theta_1 = \Delta\theta_2$, a set of the parameters is (θ_s, w_s, $\Delta\theta$, σ, $a_{\text{pl},1}$, $a_{\text{pl},2}$), which can be determined by fitting the surface pressure data, as shown in Fig. 17b. The unit of these parameters is either degree or radian. The distribution of $\Delta\bar{p}$ given by Eq. (20) fits the measurement data well in Case 1.

Figures 18a and b show the time-averaged p-field normalized by the incoming boundary layer pressure and profiles of $\Delta\bar{p}$ obtained from PSP measurements at Mach 3 with a deflection angle of 20° (Case 2) [62], respectively. The p-plateau associated with the separated flow includes a local maximum and a local minimum in the distribution of $\Delta\bar{p}$
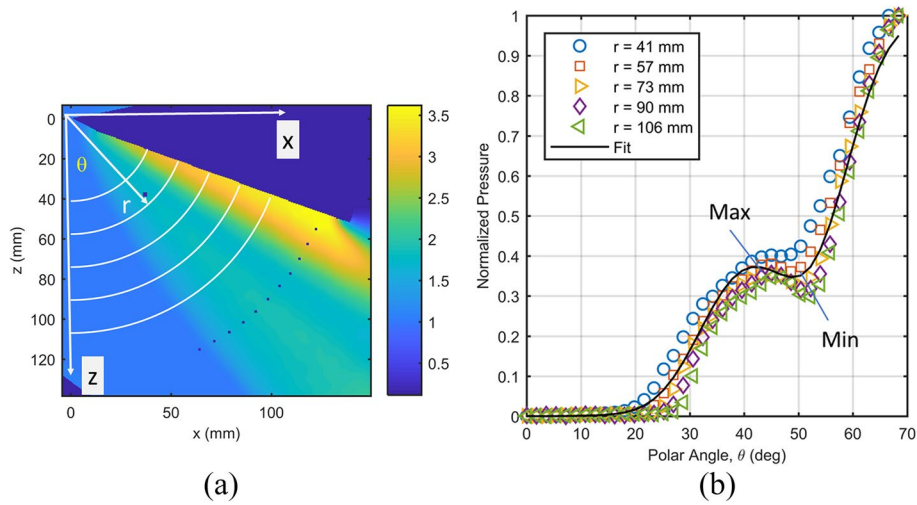
Fig. 18 PSP results in swept SWBLI at Mach 3 with a fin deflection angle of 20° [25]: **a** normalized surface pressure image by the incoming boundary layer pressure (p/p_∞), and **b** normalized surface pressure ($\Delta\bar{p}$) profiles at five radial arcs. From Liu et al. [33]

in Case 2, in contrast to the monotonic increase observed in Case 1. This surface pressure feature corresponds to the SSB, which is elucidated later. The parameters in Eq. (20) in Case 2 are determined, and the distribution of $\Delta\bar{p}$ given by Eq. (20) with these parameters fits the measurement data well in Case 2.

To investigate the topological evolution of the (τ, p)-structure as the relevant parameters vary, simulations are conducted based on the conical p-field described by Eq. (20) for Case 1. The p-plateau amplitude $a_{\mathrm{pl}} \equiv a_{\mathrm{pl},1} = a_{\mathrm{pl},2}$ is used as a control parameter since it describes the geometrical feature of the p-plateau related to the SSB. To study the effect of a_{pl}, the power-law exponent is $m = 1/5$ for the incoming turbulent boundary layer on a flat plate with a power law $\tau^{(0)} \propto (x - x_0)^{-1/5}$ and $x_0 = -1000$ pixels [33]. Thus, a field (1000×1300 pixels) of the normalized composite surface pressure $\bar{p}^{(1)} = \bar{p}^{(0)} + A_m \Delta\bar{p}$ is generated, where the p-variation amplitude is fixed at $A_m = 0.3$. Figure 19 shows the $\bar{p}^{(1)}$-surfaces for different values of a_{pl}, where the intersections at eight arcs are shown. As shown in Fig. 19, as a_{pl} increases, the $\bar{p}^{(1)}$-surface becomes folded and the p-plateau forms near the position of the inviscid shock ($\theta_s = 44.7°$). The normalized composite surface pressure $\bar{p}^{(1)} = \bar{p}^{(0)}(r\sin\theta) + A_m \Delta\bar{p}(\theta)$ does not have the exact conical similarity.

We introduce the following normalized surface pressure difference:

$$\Delta\bar{p}^{(1)} = \frac{\bar{p}^{(1)} - \min\left(\bar{p}^{(1)}\right)}{\max\left(\bar{p}^{(1)}\right) - \min\left(\bar{p}^{(1)}\right)}. \tag{22}$$

Figure 20 shows the $\Delta\bar{p}^{(1)}$-profiles at five radial arcs for different values of a_{pl}. The $\Delta\bar{p}^{(1)}$-profiles collapse in all the cases, exhibiting approximately the conical similarity. For $a_{\mathrm{pl}} = 0$, the $\Delta\bar{p}^{(1)}$-profiles show a typical monotonic surface pressure rise across a shock wave. As a_{pl} increases to 0.11, the p-plateau forms as shown in Fig. 20, which is characterized by an inflection point. Accordingly, the p-plateau corresponds to a fold on the $\bar{p}^{(1)}$-surface in Fig. 19.
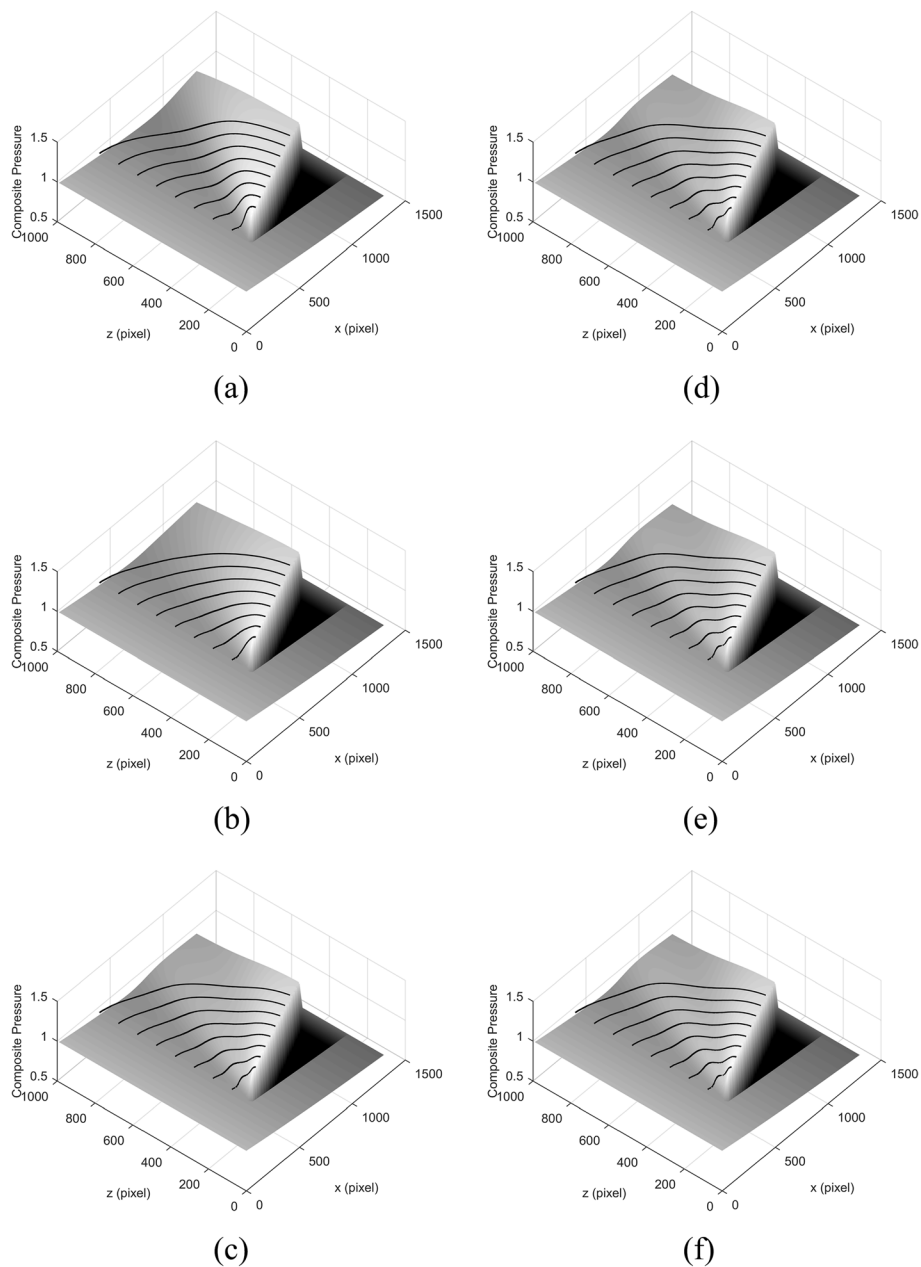
Fig. 19 The $\bar{p}^{(1)}$-surfaces and intersections at radial arcs for different values of the pressure plateau amplitude a_{pl}: **a** 0, **b** 0.05, **c** 0.095, **d** 0.1, **e** 0.105, and **f** 0.11. From Liu et al. [33]

From the $\bar{p}^{(1)}$-fields, the $\boldsymbol{\tau}^{(1)}$-fields are extracted by solving the Euler–Lagrange equation with the Lagrange multiplier $\alpha = 10^{-3}$. Figure 21 shows the evolution of the $\boldsymbol{\tau}$-topology as a_{pl} increases, which are superposed on the $\bar{p}^{(1)}$-fields as a background, respectively. For $a_{\mathrm{pl}} = 0$, the typical $\boldsymbol{\tau}$-structures are observed in swept SWBLI, where the primary separation line originates from the leading edge of the fin and an attachment line occurs near the fin-floor corner. The primary separation and attachment lines are denoted by PS and PA in Fig. 21a, respectively. The primary separation line slightly curved near the apex of the fin asymptotically approaches a straight ray line that has an
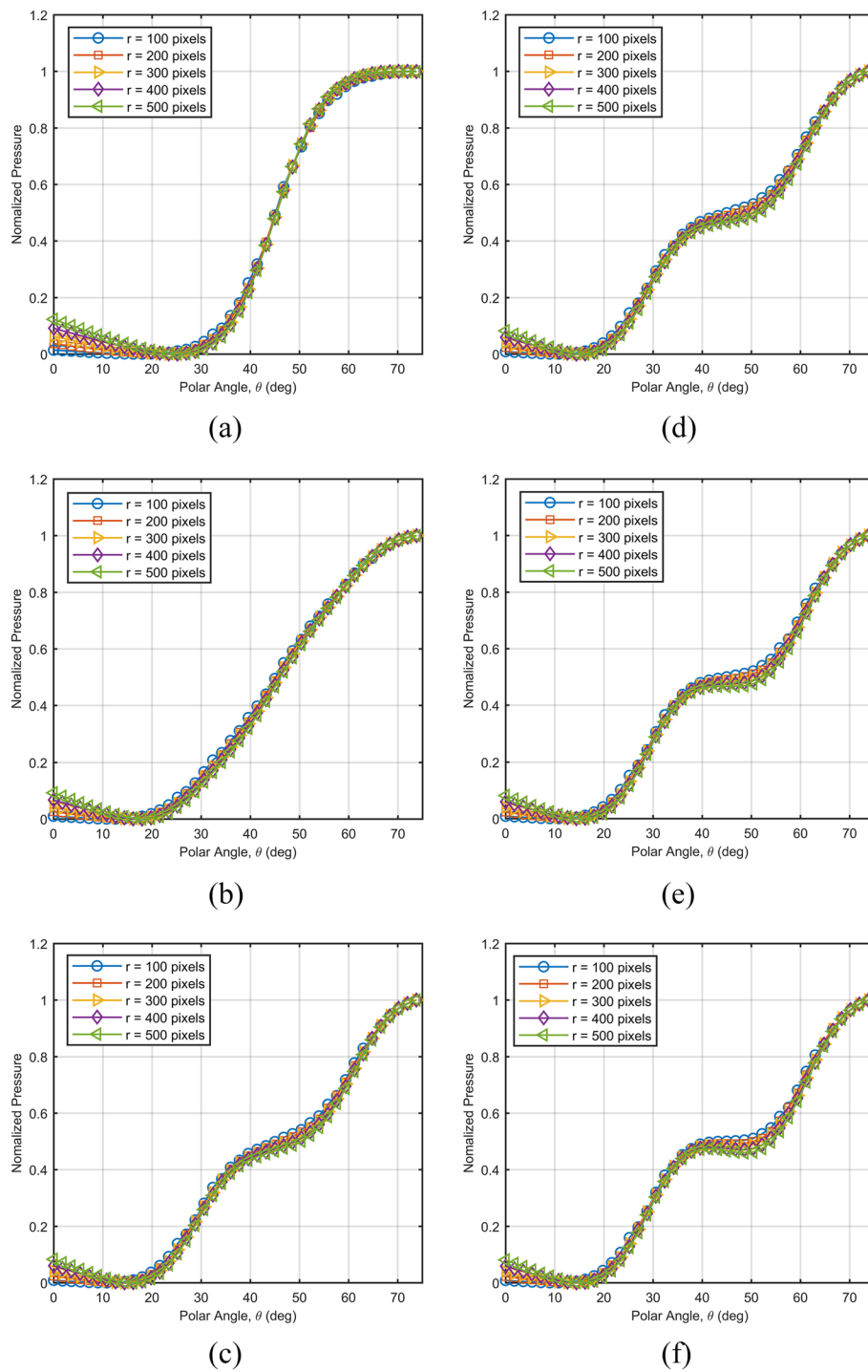
Fig. 20 The $\Delta\bar{p}^{(1)}$-profiles at five radial arcs for different values of the pressure plateau amplitude a_{pl}: **a** 0, **b** 0.05, **c** 0.095, **d** 0.1, **e** 0.105, and **f** 0.11. From Liu et al. [33]

intercept with the inviscid shock wave line that is defined as the VCO, as illustrated in Fig. 21b. Interestingly, the reconstructed $\boldsymbol{\tau}$-topology from the p-field indicates the existence of the inception zone even though the simulated p-field given by Eq. (20) is ideally conical. Here a separation line is identified as a skin friction line ($\boldsymbol{\tau}$-line) to which
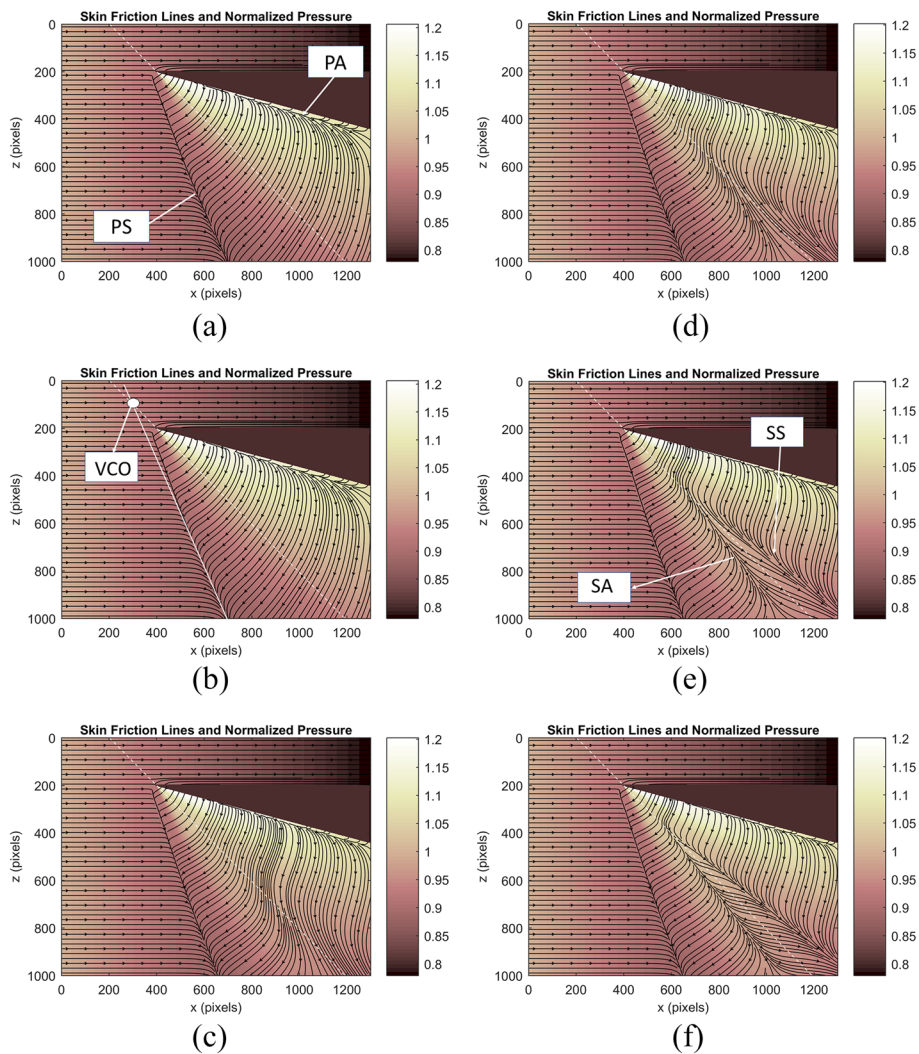
Fig. 21 Skin friction lines on the normalized composite surface pressure fields for different values of the pressure plateau amplitude a_{pl}: **a** 0, **b** 0.05, **c** 0.095, **d** 0.1, **e** 0.105, and **f** 0.11, where the dashed line indicates the position of the inviscid shock wave. PS: primary separation line, PA: primary attachment line, SS: secondary separation line, SA: secondary attachment line. From Liu et al. [33]

neighboring τ-lines converge, while an attachment line is a τ-line from which neighboring τ-lines diverge. For $a_{pl} = 0.05$, the attachment line retreats toward the fin-floor corner. As a_{pl} increases from 0.095 to 0.11, τ-lines between the primary separation line and the fin-floor corner start to deform, and the secondary separation and attachment lines form. This pair of the secondary separation and attachment lines is associated with a conical SSB. The secondary separation and attachment lines are denoted by SS and SA in Fig. 21e. The secondary separation in swept SWBLIs was observed under certain conditions in experiments and CFD simulations [57, 58]. The SSB directly corresponds to the inflection point on the *p*-curves along the radial arcs in Fig. 20. In other words, the SSB directly corresponds to a fold on the $\bar{p}^{(1)}$-surface in Fig. 19. This intrinsic correspondence between the τ-topology and the geometry of the $\bar{p}^{(1)}$-surface is imbedded in the on-wall relation Eq. (1). Based on the above observation, the SSB probably occurs

when a p-plateau (or hill-valley structure) in $\overline{\Delta p}^{(1)}$ starts to form. A heuristic condition is proposed for the formation of the SSB in swept SWBLI, i.e., $\partial(\Delta \overline{p}^{(1)})/\partial \theta = 0$ and $\partial^2(\Delta \overline{p}^{(1)})/\partial \theta^2 = 0$. Therefore, the formation of the SSB is related to specific features of the p-field, depending on the control parameters, particularly the p-plateau amplitude.

From the $\boldsymbol{\tau}$-field and p-field, the near-wall velocity field can be reconstructed by using the Taylor-series expansion solution of the NS equations that is valid in a near-wall region of about 10 wall units [22]. Figure 22 shows near-wall streamlines for different values of a_{pl}. For $a_{\mathrm{pl}} = 0 - 0.05$, streamlines are pushed upward near the primary separation line, while the primary separation bubble induces downwash streamlines near the attachment line near the fin surface. For $a_{\mathrm{pl}} = 0.095 - 0.11$, the upward streamlines occur near the secondary separation line and the downwash streamlines appear near the secondary attachment line.

6 Conclusions

The approximate method is developed for reconstruction of the skin friction topology and near-wall velocity field in complex separated flows. This is a constructive method in a mathematical sense based on the exact relation between skin friction ($\boldsymbol{\tau}$) and surface pressure (p) (simply called the ($\boldsymbol{\tau}, p$)-relation) derived from the NS equations with the boundary enstrophy flux (BEF) as a key link. This approximate method has several related technical aspects. First, the composite surface pressure field is given by a linear superposition of the base-flow surface pressure field and the surface pressure variation field. Then, under the first-order approximation where the base-flow BEF field is used, the first-order skin friction field ($\boldsymbol{\tau}$-field) can be determined from the composite surface pressure field by solving the Euler–Lagrange equation. Further, the near-wall velocity field is reconstructed from the extracted $\boldsymbol{\tau}$- and p-fields by using the Taylor-series expansion solution of the NS equations. In addition, the Poincare-Bendixson index formula (the P-B formula) provides a topological constraint on the reconstructed $\boldsymbol{\tau}$-field for examining its topological consistency.

In simulations, the approximate method is applied to reconstruction of some elemental ($\boldsymbol{\tau}, p$)-structures ($\boldsymbol{\tau}$-source/sink, $\boldsymbol{\tau}$-vortex and their combinations) when some simple forms of the surface pressure variation are imposed on the base flow with the power-law distributions of skin friction, surface pressure and BEF (the Falkner-Skan flow in this case). The distinct topological features like critical points and separation/attachment lines are revealed, and the critical points in these structures are topologically consistent, satisfying the P-B formula. Furthermore, complex ($\boldsymbol{\tau}, p$)-structures in shock-wave/boundary-layer interactions (SWBLIs) and the delta-wing flow are reconstructed to exhibit typical 3D flow separations.

In experiments, the approximate method is applied to unsteady PSP images obtained in incident SWBLI. The high-resolution $\boldsymbol{\tau}$-fields are extracted from a time sequence of PSP images at different Reynolds numbers, clearly revealing the detailed structures characterized by the separation and attachment lines of the separation bubble induced by the incident shock wave. The time-averaged, normalized $\boldsymbol{\tau}$-fields extracted from PSP images agree with the data obtained by surface shear sensitive film (S3F).
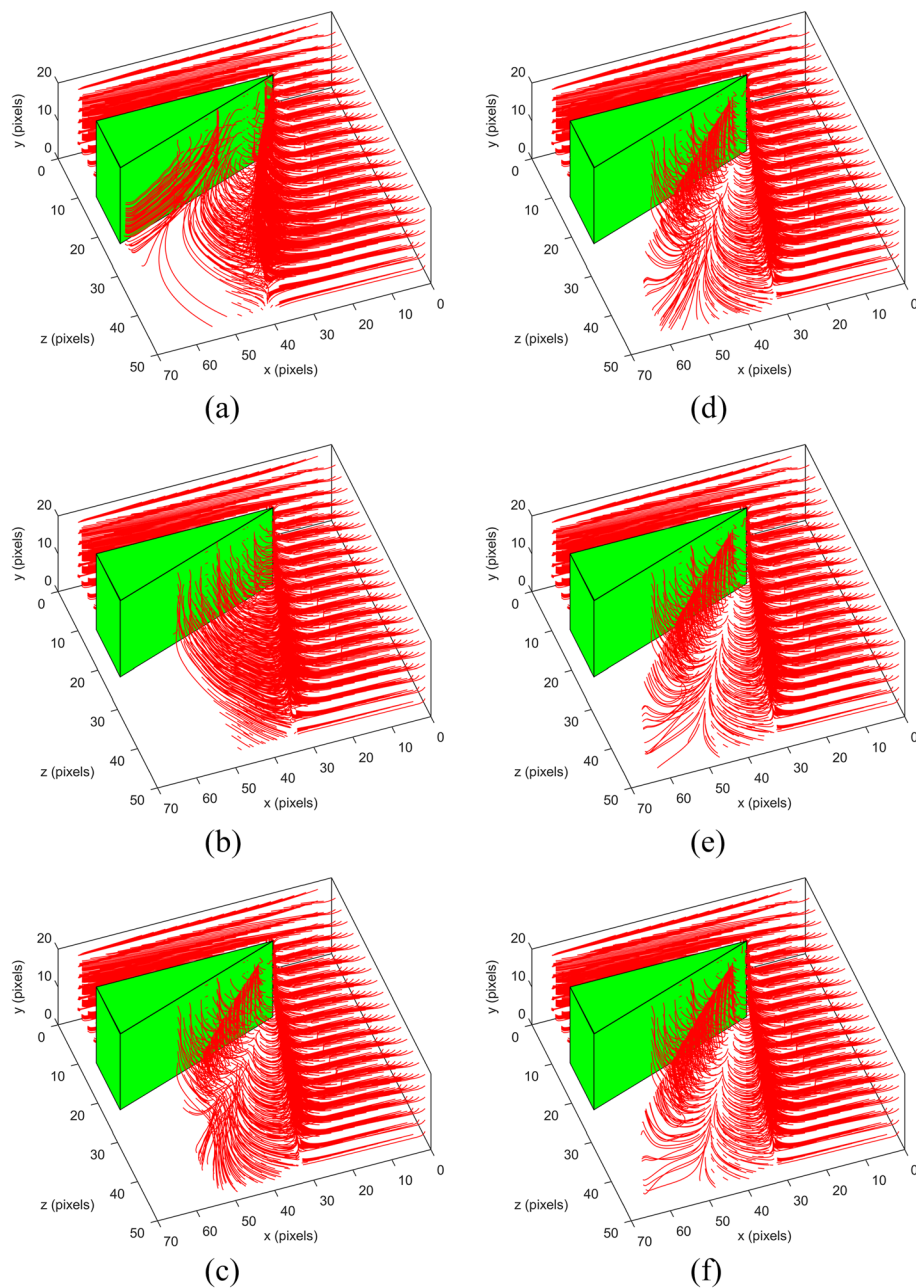
Fig. 22 Near-wall streamlines for different values of the pressure plateau amplitude a_{pl}: **a** 0, **b** 0.05, **c** 0.095, **d** 0.1, **e** 0.105, and **f** 0.11. From Liu et al. [33]

Further, by using the approximate method, the relationship between the τ-topology and p-field in fin-generated swept SWBLIs is studied, focusing on the formation of the secondary separation bubble (SSB). The formation of the SSB is directly related to the p-plateau amplitude that controls the p-surface geometry in a 3D space. As the p-plateau amplitude increases, the p-surface is folded near the inviscid shock location, leading to a pair of separation and attachment lines associated with the SSB in the τ-field. The formation of the SSB is related to the specific features of the p-field, depending on the control parameters, particularly the p-plateau amplitude.

Declarations

Availability of data and materials
Not applicable.

Competing interests
No competing interest.

References

1. Legendre R (1956) Separation de l'ecoulement laminaire tridimensionnel. Rech Aeronaut 54:3–8
2. Lighthill MJ (1963) Attachment and separation in three-dimensional Flow. In: Rosenhead L (ed) Laminar boundary layers, Section II 2.6. Oxford University Press, Oxford, pp 72–82
3. Wang KC (1974) Boundary layer over a blunt body at high incidence with an open-type separation. Proc R Soc Lond A 340:33–55. https://doi.org/10.1098/rspa.1974.0139
4. Hunt JCR, Abell CJ, Peterka JA et al (1978) Kinematical studies of the flows around free or surface-mounted obstacles: applying topology to flow visualization. J Fluid Mech 86(1):179–200. https://doi.org/10.1017/S0022112078001068 0 68
5. Tobak M, Peake DJ (1982) Topology of three-dimensional separated flows. Annu Rev Fluid Mech 14:61–85. https://doi.org/10.1146/annurev.fl.14.010182.000425
6. Dallmann U (1983) Topological structures of three-dimensional vortex flow separation. In: 16th fluid and plasmadynamics conference, Danvers, 12-14 July 1983. https://doi.org/10.2514/6.1983-1735
7. Hornung H, Perry AE (1984) Some aspects of three-dimensional separation. I: Streamsurface bifurcation. Z Flugwiss Weltraumforsch 8(2):77–87
8. Zhang HX (1985) The separation criteria and flow behaviour for three-dimensional steady separated flow. Acta Aerodyn Sin 1:1–12 (in Chinese)
9. Perry AE, Chong MS (1987) A description of eddying motions and flow patterns using critical-point concepts. Annu Rev Fluid Mech 19:125–155. https://doi.org/10.1146/annurev.fl.19.010187.001013
10. Chapman GT, Yates LA (1991) Topology of flow separation on three-dimensional bodies. Appl Mech Rev 44(7):329–345. https://doi.org/10.1115/1.3119507
11. Hsieh T, Wang KC (1996) Three-dimensional separated flow structure over a cylinder with a hemispherical cap. J Fluid Mech 324:83–108. https://doi.org/10.1017/S0022112096007847
12. Délery JM (1992) Physics of vortical flows. J Aircr 29(5):856–876. https://doi.org/10.2514/3.46256
13. Délery JM (2001) Robert Legendre and Henri Werlé: toward the elucidation of three-dimensional separation. Annu Rev Fluid Mech 33:129–154. https://doi.org/10.1146/annurev.fluid.33.1.129
14. Foss JF (2004) Surface selections and topological constraint evaluations for flow field analyses. Exp Fluids 37:883–898. https://doi.org/10.1007/s00348-004-0877-0
15. Foss JF (2007) Topological considerations in fluid mechanics measurements. In: Tropea C, Yarin AL, Foss JF (eds) Springer handbook of experimental fluid mechanics. Springer, Berlin, Heidelberg. https://doi.org/10.1007/978-3-540-30299-5_13
16. Ma T, Wang S (2001) A generalized Poincaré–Hopf index formula and its applications to 2-D incompressible flows. Nonlinear Anal Real World Appl 2(4):467–482. https://doi.org/10.1016/S1468-1218(01)00004-9
17. Liu T, Woodiga S, Ma T (2011) Skin friction topology in a region enclosed by penetrable boundary. Exp Fluids 51:1549–1562. https://doi.org/10.1007/s00348-011-1171-6
18. Firby PA, Gardiner CF (2001) Vector fields on surfaces. In: Surface topology, 3rd edn. Woodhead Publishing Limited, Cambridge
19. Kinsey LC (1993) Topology and calculus. In: Topology of surfaces. Undergraduate Texts in Mathematics. Springer, New York

20. Perry AE, Chong MS (1986) A series-expansion study of the Navier–Stokes equations with applications to three-dimensional separation patterns. J Fluid Mech 173:207–223. https://doi.org/10.1017/S0022112086001143

21. Bewley TR, Protas B (2004) Skin friction and pressure: the "footprints" of turbulence. Physica D 196(1–2):28–44. https://doi.org/10.1016/j.physd.2004.02.008

22. Chen T, Liu T, Dong ZQ et al (2021) Near-wall flow structures and related surface quantities in wall-bounded turbulence. Phys Fluids 33(6):065116. https://doi.org/10.1063/5.0051649

23. Liu T, Misaka T, Asai K et al (2016) Feasibility of skin-friction diagnostics based on surface pressure gradient field. Meas Sci Technol 27:125304. https://doi.org/10.1088/0957-0233/27/12/125304

24. Chen T, Liu T, Wang LP et al (2019) Relations between skin friction and other surface quantities in viscous flows. Phys Fluids 31(10):107101. https://doi.org/10.1063/1.5120454

25. Liu T (2013) Extraction of skin-friction fields from surface flow visualizations as an inverse problem. Meas Sci Technol 24:124004. https://doi.org/10.1088/0957-0233/24/12/124004

26. Liu T (2019) Global skin friction measurements and interpretation. Prog Aerosp Sci 111:100584. https://doi.org/10.1016/j.paerosci.2019.100584

27. Wu JZ, Tramel RW, Zhu FL et al (2000) A vorticity dynamics theory of three-dimensional flow separation. Phys Fluids 12(8):1932–1954. https://doi.org/10.1063/1.870442

28. Wu JZ, Ma HY, Zhou MD (2006) Vorticity dynamics in flow separation. In: Vorticity and vortex dynamics. Springer Berlin, Heidelberg, pp 201–252

29. Surana A, Grunberg O, Haller G (2006) Exact theory of three-dimensional flow separation. Part 1. Steady separation. J Fluid Mech 564:57–103. https://doi.org/10.1017/S0022112006001200

30. Surana A, Jacobs GB, Haller G (2007) Extraction of separation and attachment surfaces from three-dimensional steady shear flows. AIAA J 45(6):1290–1302. https://doi.org/10.2514/1.21464

31. Liu T (2018) Skin-friction and surface-pressure structures in near-wall flows. AIAA J 56(10):3887–3896. https://doi.org/10.2514/1.J057216

32. Liu T, Salazar DM, Crafton J et al (2021) Skin friction extracted from surface pressure in incident shock-wave/boundary-layer interaction. AIAA J 59(10):3910–3922. https://doi.org/10.2514/1.J060345

33. Liu T, Salazar DM, Mears LJ et al (2022) Relationship between secondary separation and surface pressure structure in swept shock-wave/boundary-layer interaction. Shock Waves 32:665–678. https://doi.org/10.1007/s00193-022-01102-5

34. Tikhonov AN, Arsenin VY (1977) Solutions of ill-posed problems. Halsted Press, New York

35. Horn BKP, Schunck BG (1981) Determining optical flow. Artif Intell 17(1-3):185–203. https://doi.org/10.1016/0004-3702(81)90024-2

36. Liu T, Shen L (2008) Fluid flow and optical flow. J Fluid Mech 614:253–291. https://doi.org/10.1017/S0022112008003273

37. Wang B, Cai Z, Shen L et al (2015) An analysis of physics-based optical flow. J Comput Appl Math 276:62–80. https://doi.org/10.1016/j.cam.2014.08.020

38. Schlichting H (1979) Boundary-layer theory, 7th edn. McGraw-Hill, New York

39. Ishak A, Nazar R, Pop I (2007) Falkner-Skan equation for flow past a moving wedge with suction or injection. J Appl Math Comput 25(1–2):67–83. https://doi.org/10.1007/BF02832339

40. Chen Y (2017) Theoretical and numerical study on vorticity dynamics of flow with deformable boundary. Dissertation, Fudan University

41. Chong MS, Monty JP, Chin C et al (2012) The topology of skin friction and surface vorticity fields in wall-bounded flows. J Turbul 13:N6. https://doi.org/10.1080/14685248.2012.663093

42. Lenaers P, Li Q, Brethouwer G et al (2012) Rare backflow and extreme wall-normal velocity fluctuations in near-wall turbulence. Phys Fluids 24(3):035110. https://doi.org/10.1063/1.3696304

43. Brücker Ch (2015) Evidence of rare backflow and skin-friction critical points in near-wall turbulence using micropillar imaging. Phys Fluids 27(3):031705. https://doi.org/10.1063/1.4916768

44. Husen NM, Liu T, Sullivan JP (2018) Luminescent oil film flow tagging skin friction meter applied to FAITH hill. AIAA J 56(10):3875–3886. https://doi.org/10.2514/1.J057114

45. van den Berg B (1997) Physical aspects of separation in three-dimensional flows. National Aerospace Laboratory NLR TP 97127

46. McLean D (2012) Understanding aerodynamics. Wiley, New York

47. Knight D, Yan H, Panaras AG et al (2003) Advances in CFD prediction of shock wave turbulent boundary layer interactions. Prog Aerosp Sci 39(2-3):121–184. https://doi.org/10.1016/S0376-0421(02)00069-6

48. Borovoy V, Egorov I, Maximenko A et al (2013) Three-dimensional shock-wave/boundary-layer interaction at the presence of entropy layer. Prog Flight Phys 5:327–348. https://doi.org/10.1051/eucass/201305327

49. Lu Fk (1993) Quasiconical free interaction between a swept shock and a turbulent boundary layer. AIAA J 31(4):686–692. https://doi.org/10.2514/3.11604

50. Woike MR, Davis DO, Clem MM et al (2017) The investigation of shock wave boundary layer interactions using fast pressure sensitive paint and surface stress sensitive film measurement techniques. In: 33rd AIAA aerodynamic measurement technology and ground testing conference, Denver, 5-9 June 2017. https://doi.org/10.2514/6.2017-3732

51. Davis DO (2015) CFD validation experiment of a Mach 2.5 axisymmetric shock-wave/boundary-layer interaction. In: Proceedings of the ASME/JSME/KSME 2015 joint fluids engineering conference. Volume 1: Symposia. Seoul, 26-31 July 2015. https://doi.org/10.1115/AJKFluids2015-6342

52. Pirozzoli S, Bernardini M (2011) Direct numerical simulation database for impinging shock wave/turbulent boundary-layer interaction. AIAA J 49(6):1307–1312. https://doi.org/10.2514/1.J050901

53. Liu T, Sullivan JP, Asai K et al (2021) Pressure and temperature sensitive paints, 2nd edn. Springer, Cham

54. Babinsky H, Harvey JK (2011) Shock wave-boundary-layer interactions. Cambridge University Press, Cambridge. https://doi.org/10.1017/CBO9780511842757

55. Délery J, Dussauge JP (2009) Some physical aspects of shock wave/boundary layer interactions. Shock Waves 19:453–468. https://doi.org/10.1007/s00193-009-0220-z

56. Dolling DS (2001) Fifty years of shock-wave/boundary-layer interaction research: what next? AIAA J 39(8):1517–1531. https://doi.org/10.2514/2.1476
57. Panaras AG (1996) Review of the physics of swept-shock/boundary-layer interactions. Prog Aerosp Sci 32(2-3):173–244. https://doi.org/10.1016/0376-0421(95)00005-4
58. Zheltovodov A (1996) Shock-waves/turbulent boundary-layer interactions: fundamental studies and applications. In: AIAA fluid dynamics conference, New Orleans, 17-20 June 1996. https://doi.org/10.2514/6.1996-1977
59. Van Oudheusden BW, Nebbeling C, Bannink WJ (1996) Topological interpretation of the surface flow visualization of conical viscous/inviscid interactions. J Fluid Mech 316:115–137. https://doi.org/10.1017/S0022112096000468
60. Settles GS, Lu FK (1985) Conical similarity of shock/boundary-layer interactions generated by swept and unswept fins. AIAA J 23(7):1021–1027. https://doi.org/10.2514/6.1983-1756
61. Mears LJ, Baldwin A, Ali MY et al (2020) Spatially resolved mean and unsteady surface pressure in swept SBLI using PSP. Exp Fluids 61:92. https://doi.org/10.1007/s00348-020-2924-x
62. Baldwin AK (2021) Experimental characterization and flowfield analysis of a swept shock-wave/boundary-layer interaction. Dissertation, Florida State University

Publisher's Note

Springer Nature remains neutral with regard to jurisdictional claims in published maps and institutional affiliations.